THE USE OF AFM INDENTATION TO QUANTIFY MECHANICAL PROPERTIES OF THE INTERPHASE REGION IN FIBER-REINFORCED COMPOSITES

By

LIBIN KALEELUVILAYIL BABU

Bachelor of Technology in Mechanical Engineering
University of Kerala
Thiruvananthapuram, Kerala, India
2012

Master of Science in Mechanical and Aerospace Engineering
Oklahoma State University
Stillwater, OK, USA
2015

Submitted to the Faculty of the
Graduate College of
Oklahoma State University
in partial fulfillment of
the requirements for
the Degree of
Doctor of Philosophy
July, 2019

THE USE OF AFM INDENTATION TO QUANTIFY MECHANICAL PROPERTIES OF THE INTERPHASE REGION IN FIBER-REINFORCED COMPOSITES

Dissertation Approved:

Dr. Raman P. Singh

Dissertation Advisor

Dr. Khaled A. Sallam

Dr. Shuodao Wang

Dr. DoYoung Kim

ACKNOWLEDGMENTS

First and foremost, I am grateful to my God for the blessings to do the PhD program and for arranging the best people to provide guidance and motivation.

I am very thankful to my advisor, Dr. Raman P. Singh, whose encouragement, supervision and support from the preliminary to the concluding step has enabled me to develop an understanding of the subject. It would have been next to impossible to do this research and write this dissertation without the guidance of Dr. Singh. Greatly indebted for his patience and financial support provided towards my research work.

I would like to express my gratitude to Dr. Sallam, Dr. Wang and Dr. Kim for their precious time and support throughout my research work and for being a part of my PhD defense committee.

Thank you to Dr. Mishra for his continuous cooperation in each and every step. He was always there with his helping hand whenever I felt the need for his expertise. Also, I am grateful to Dr. Hamim for his advice and motivation at different steps of this PhD work.

My lab–mates and colleagues helped and supported me always in the thick and thin phase of these 6 years at OSU. In particular, I want to express gratitude to my current lab members Blaze and Tharun for their assistance and cooperation. I would also like to thank my friends Ranjan, Padmanapan and all others at HRC for their support, chat, gossip and our random discussion. Sincere thanks to front desk staff, Julia and core lab in-charge Dr. Lu for all the help provided.

Lastly, I am thankful to my wife, my son, my parents, my in-laws, my brother and all my relatives who have always encouraged and prayed for me during this journey of PhD program.

Acknowledgements reflect the views of the author and are not endorsed by committee members or Oklahoma State University.

Name: LIBIN KALEELUVILAYIL BABU

Date of Degree: JULY, 2019

Title of Study: THE USE OF AFM INDENTATION TO QUANTIFY MECHANICAL PROPERTIES OF THE INTERPHASE REGION IN FIBER-REINFORCED COMPOSITES

Major Field: MECHANICAL AND AEROSPACE ENGINEERING

Interphase is the region in the vicinity of the reinforcing fiber in the polymer composites with properties distinct from the bulk matrix. Investigation of these nano- and micro-interphase regions have been done using conventional indentation techniques, followed by closed form solutions applicable to the indentation in a semi-infinite space. However, due to the presence of the fiber the interphase region can be considered only as a semi-infinite space with rigid constraint. An integrated approach using AFM (Atomic Force Microscopy) based indentation and FEA (Finite Element Analysis) is used to investigate the effect of the fiber constraint on the mechanical properties of the interphase region. Obtained results indicate that the thickness of the interphase region is approximately 250 nm, based on the gradient in the elastic modulus as a function of radial distance from the fiber. 3D FEA using an elasto-plastic material model indicates that the fiber constraint effect is considerable in the region less than 40 nm away from the fiber. The time-dependent behavior of the interphase region is studied using constant displacement approach, and the distinct viscoelastic response of the interphase region is observed as a function of the radial distance to the fiber. FEA using a linear viscoelastic material model shows that the influence of fiber constraint on the evaluation of the viscoelastic properties is distinguishable only within 20 nm away from the fiber. Due to the limited extent of influence of fiber constraint effect, the distinct behavior of the interphase region in terms of elastic and viscoelastic properties is confirmed. Additionally, it is shown that consideration of an axi–symmetry assumption for modeling the interphase region leads to an overestimation of the properties of the region. This technique is further implemented to demonstrate the effect of UV irradiation on the interphase region. Methodical analysis of the data indicates that the response of epoxy to UV irradiation is influenced by the proximity to the reinforcement and carbon fiber reinforcement hinders the photo-degradation of epoxy. Furthermore, the influence of the thermal mismatch between the fiber and the matrix on the formation of the interphase and the effect of post–curing are examined using the approach considered in this study. Results indicate that the presence of thermal stresses greatly impact the width of the interphase region and its behavior.

TABLE OF CONTENTS

LIST OF TABLES

Table Page

LIST OF FIGURES

CHAPTER 1

INTRODUCTION

Fiber-reinforced polymer-matrix composites find extensive application across various sectors including transportation, energy generation, aerospace, and infrastructure. This can be attributed to the exceptional properties of composite materials such as high strength to weight ratio and high modulus [3, 4]. Furthermore, the design and fabrication process can be tailored to generate direction-dependent material properties [5]. Nonetheless, understanding and predicting the influence of near-fiber region on the long-term durability of composite materials and its performance under harsh environments continues to be a matter of concern [6–8]. Characterizing the mechanical response, damage tolerance, and long-term durability of these materials is further complicated because it involves the response of the two individual components, namely the fiber and the matrix, and also by the interaction between the two.

This study is focused on the near-fiber region known as interphase (illustrated in Fig. 1.1), which is often characterized by a matrix material with properties distinct from the rest of the bulk material [9–11]. Its presence is a result of the chemical interaction between the fiber and the matrix, during the curing process in composites [12]. The response of the interphase region governs the load-transfer mechanisms in composites and can be considered as an important determinant of the type of failure and the overall load bearing capabilities of the composite material [6, 13]. The following sections discuss the challenges associated with the determination of true properties of the interphase region at very small length scales.

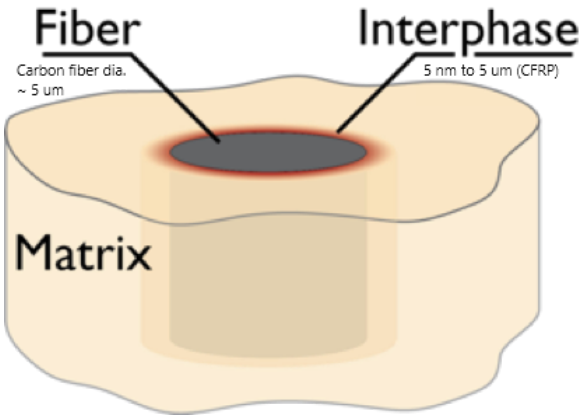

Figure 1.1: Schematic illustration of the interphase region in composites.

1.1 Literature review about the interphase region

1.1.1 Span and characterization of the fiber–matrix interphase

The interphase properties as well as its width are dependent on the materials considered and can be influenced by fiber surface treatments [14–16]. The width of the interphase region in polymer-matrix composites has been found to vary from several hundred nanometers to few micrometers, depending on the chemical interaction between the fiber and the matrix [17–19]. Many studies have characterized the effect addition of nanoparticles in polymer composites and its overall behavior [20–25]. However, due to the small length scale of the interphase region, several nanomechanical methods based on tip–specimen interaction have been prominence in the characterization of the interphase region. These include instrumented nanoindentation [26, 27], nano-scratch techniques [28], and atomic force microscope (AFM) indentation [29–33]. Nonetheless, the application of the above described methods to determine the mechanical properties of the interphase region is limited by the assumption of an unconstrained space, as all of the solutions available are for indentation in a semi-infinite half-space as shown in Fig. 1.2 [34]. In this context, it is instructive to examine the effectiveness of the techniques used in indentation to evaluate material properties such as elastic modulus.

Considering the small-scale width of the interphase region which varies from nano

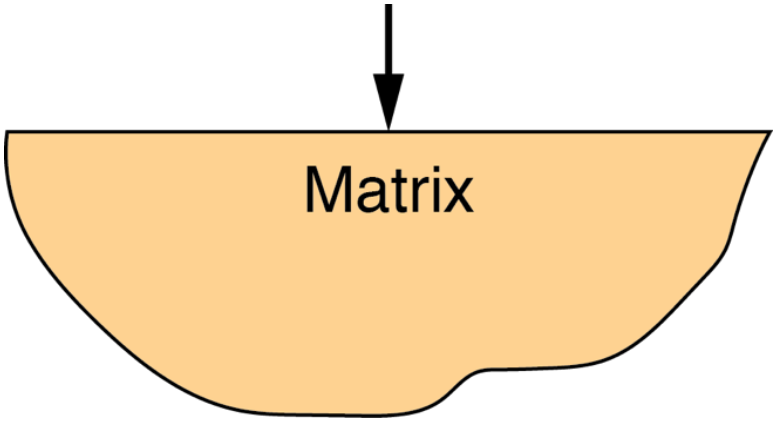

Figure 1.2: Point load on semi infinite elastic space.

scale to few microns, indentation methods have proved to be a versatile tool in the evaluation of its properties. Munz *et al.* [35] found that the thickness of the interphase region in carbon fiber–epoxy system was about 20–80 nm using an AFM indentation technique. Nano-scratch testing was used by Kim *et al.* [36] to find the width of the interphase in glass fiber reinforced–vinyl composites and nanoindentation was used by Lee *et al.* [37] to estimate the transition zone in cellulose fiber reinforced polypropylene. Wang *et al.* [38] used AFM characterization techniques to study the interfacial properties of carbon reinforced composites that were subjected to hygrothermal treatments. Topographic changes and phase images were used to show the reduction in the height as samples were exposed to hygroscopic treatments. Reynaud *et al.* [39] determined the Young's modulus of a biphase polymer system using AFM. Despite a fair number of studies done over nearly two decades it is instructive to examine details of the indentation process in order to determine the effectiveness of the techniques *in quantifying the properties* of the interphase phase region.

1.1.2 Evaluation of material properties using indentation technique

The main components of a nanoindentation system include an indenter and a force generation source possessing controlling capabilities coupled with a data acquisition tool. The primary purpose behind the development of nanoindentation was to analyze materials of relatively smaller volume, such as thin films on substrates, with the ability to indent at

micron and submicron length-scales. The contact theory used along with indentation technique to determine mechanical properties such as elastic modulus and hardness is briefly discussed as follows.

In 1885, Boussinesq developed the solution for a concentrated load applied on a semi-infinite elastic space. Relationships for deformations and stresses along the three directions were derived in terms of material constants, elastic modulus (E) and Poisson's ratio (ν).

The relationship between the applied load and the indenter displacement was derived by Sneddon [40],

$$P = \alpha h^m \tag{1.1}$$

where, P and h are the load and displacement, respectively and α and m are power law fitting constants.

Doerner and Nix [41] in 1991, proposed an extensive method to evaluate the contact area utilizing the shape of the indenter. Based on this work, mechanical properties such as elastic modulus and hardness could be computed using the contact load at the point of maximum loading utilizing Sneddon's solution for elastic indentation. Doerner and Nix considered the elastic behavior constituting the initial unloading region to be linear and therefore assumed the contact area to be constant. Oliver and Pharr [34] raised concerns about this assumption stating that constant contact area during unloading doesn't hold true for all materials. They proposed that unloading curve could be characterized using a power law. This led to the development of a method that is seen as the most widely employed tool for evaluating the elastic modulus and hardness of samples subjected to nanoindentation. The contact depth between the indenter and substrate, h_c is given as,

$$h_c = h_{max} + \varepsilon \frac{P_{max}}{S} \tag{1.2}$$

where, P_{max} and h_{max} are the maximum indentation load and displacement, respectively. The contact stiffness S, is given by the slope of the unloading curve, dP/dh. ε is a geomet-

ric constant dependent on the indenter. For flat punch, $\varepsilon = 1$ and for conical indenters, it is evaluated as 0.75. Projected contact area at maximum load A_c is obtained as,

$$A_c = F(h_c) \tag{1.3}$$

where, $F(h_c)$ is determined by calibration of the indenter. For Berkovich indenter, $A_c = 24.5{h_c}^2$. The effective elastic modulus, E_{eff}, can be determined as,

$$S = \beta \frac{2}{\sqrt{\pi}} E_{eff} \sqrt{A_c} \tag{1.4}$$

where, the effective elastic modulus, E_{eff}, takes into consideration the elastic deformation in indenter and sample. It is related to the known indenter modulus, E_i, and Poisson's ratio, ν_i, and unknown sample modulus, E, and Poisson's ratio, ν, as,

$$\frac{1}{E_{eff}} = \frac{1-\nu^2}{E} + \frac{1-{\nu_i}^2}{E_i} \tag{1.5}$$

For indentation of time dependent materials, creep behavior leads to the formation of a "nose" at the point of unloading from maximum load. In this case, the Oliver–Pharr method overestimates the elastic modulus. Feng and Ngan developed an extension that accounts the time dependency of the material's response [42]. The relation between the true stiffness S and the apparent stiffness S_u is given as,

$$\frac{1}{S} = \frac{1}{S_u} + \frac{\dot{h}_h}{\dot{P}} \tag{1.6}$$

where, $\dot{h}_h$ is the indenter displacement rate at the end of the hold time and $\dot{P}$ is the rate of unloading at the beginning of unload curve. The true stiffness is used to determine the elastic modulus of the sample, as the modulus of the indenter is known.

It is vital to note that the application of the above described methods to determine the mechanical properties of the interphase region is limited by the assumption of un-

constrained space, as all of the preceding solutions are for indentation in a semi-infinite half-space. In the case of indentation in the interphase region, the loading is applied in the vicinity of a rigid boundary (note that the elastic modulus of fiber is very large as compared to the matrix), as indicated in Fig. 1.3. This produces a constraint effect or a fiber-bias in the indentation data, which requires the use of appropriate solutions to determine material properties from the load versus displacement data. However, most indentation studies on the behavior of interphase region completely ignore or only partially address the influence of the fiber constraint.

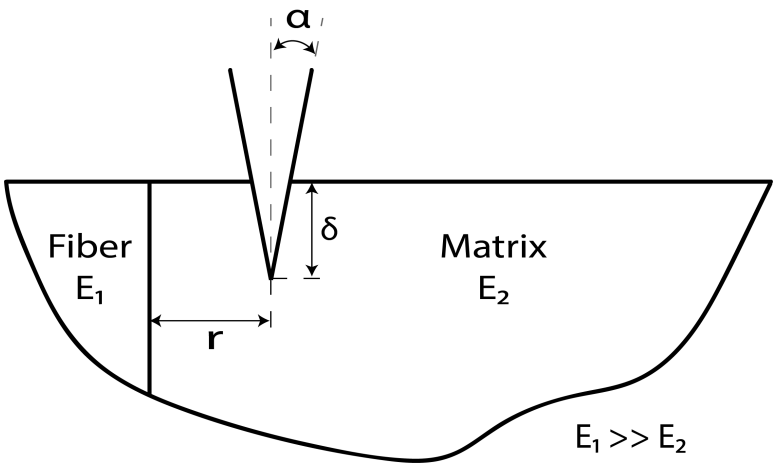

Figure 1.3: Schematic of indentation in interphase region.

Stresses produced in the material during indentation interact with the rigid boundary condition produced by the vicinity of the fiber. This leads to the overestimation of the mechanical properties in the region. Kumar *et al.* [43] described this as a phenomena due to the slowing down in the uniform flow of the bulk material, just below the indent near the stiffer fiber. Pascual *et al.* [44] pointed out that the interaction of the stress fields beneath the indenter and the nearby fiber can lead to a wrong estimation of the thickness of the interphase. Li *et al.* [45] used FEA simulations to illustrate the fiber constraint effect present during nanoindentation in the interphase region of carbon fiber–epoxy resin system. They described that there is a 'mutation' of the load–displacement curve due to a fiber stiffening effect. It was noted that the effect of variation in modulus of matrix is

negligible, but this variation was very sensitive to changes in indentation depth. Khanna *et al.* [46] evaluated the interphase behavior of silane coated glass fiber-reinforced polymer composites and suggested that the fiber constraint effect impacts the determination of the interphase properties. Li *et al.* [47] noted that indent affected zone (IAZ) is high due to the large surface radius of the indenter, in their study using conical indenter on the interphase formed by epoxy and aluminum. They added that IAZ increases proportionally to the indentation depth. Finally, Hu *et al.* [48, 49] discussed about an apparent gradient in the modulus of the fiber–matrix interphase region due to the fiber constraint. They also observed that fiber bias is directly proportional to the depth of indentation. The lack of a good contact theory for indentation of anisotropic and non-homogeneous materials was acknowledged. *While these studies acknowledge the effect of constraint on the indentation results they do not provide an explicit scheme for quantifying this effect or for decoupling the fiber-bias effect from the actual variation in the interphase properties.*

Studies by Hardiman *et al.* [1, 50] suggested the concept of a 'fiber constraint factor' (FCF) to evaluate suitable indentation depths at which fiber bias can be ignored. FCF was defined as the ratio of radius of the matrix pocket formed by surrounding fibers (R_p) to the instantaneous indentation depth (h). It was found that fiber constraint effect led to an apparent increase in modulus values of the near-fiber region by about 40–50%, and is given as,

$$FCF = \frac{R_p}{h} \tag{1.7}$$

Using FEA model of Berkovich nanoindentation, they determined that when FCF is equal to or greater than 20, the modulus values are considered to be unconstrained. Optical imaging techniques were used to determine the radius of matrix pocket. It was noted that at an indentation depth of $2\mu m$, the impression created by Berkovich indenter will extend to about 6 to $9\mu m$ from initial contact point. So, when the radius of matrix pocket is less than extension of the impression created, the indenter tip is in direct contact with the fiber.

However, the FCF considered in their work is influenced by the circularity of the matrix pockets. Also, *their work is limited to a Berkovich indenter, which has a much greater effective cone angle as compared to an AFM tip.*

1.2 Motivation for this study

Recently, Belec and Joliff [30] noted the impact of actual probe geometry on the mechanically affected zone in AFM force measurements. Brune *et al.* [51] conducted direct measurements of the stiffness of rubber interphase and indicated the possible impact of 'probe effect along with wall effect' on the interphase measurements. A recent review by Roy *et al.* [52] on the characterization of polymer nanocomposites noted the challenge in eliminating artifiacts from the interphase measurements and also remarked that AFM measurements along with Finite Element (FE) modeling will be able to overcome these challenges. Very recently, adaptive optimization technique using numerical modeling is presented as a possible method to study the interphase properties in polymer nanocomposites by Wang *et al.* [53].

Majority of the studies done on investigating the fiber–constraint effect are limited in two aspects. First, these studies have only focused on the use of a Berkovich indenter. Second, the studies have focused on elastic or elasto-plastic deformation. Addressing these limitations is the focus of the current investigation.

Objective

This aim of this research is to conduct a systematic study of the interphase region in the fiber reinforced polymer composites. AFM-based indentation due to its high spatial resolution will be employed in this study. Furthermore, to determine the influence of fiber–constraint on the interphase properties using indentation technique, a numerical approach is proposed. Additionally, effect of fiber–constraint on the viscoelastic behavior of the near fiber region will be examined using a similar approach. Finally, the technique will be used to assess

the impact of severe environmental conditions such as UV irradiation on the nano-scale properties of the region around the fiber along a radial line from the boundary of the fiber.

The load–displacement curves are the output of the indentation experiments. But the concern is that we are not certain about the material parameters in the interphase (input) that provides us the output. Therefore, it is hypothesized that the FE method can be used to analyze the effect of the fiber constraint alone on the nano-scale mechanical properties of the interphase region in composites - both from an elastoplastic and viscoelastic perspective. This numerical approach will help to evaluate any damage due to loading or environmental changes, studied using indentation technique. Major objectives of the research and approach is presented below:

- **Replicate the work done by Hardiman *et al.* [1]**: This aim of this step is to confirm the influence of fiber bias during indentation at near fiber region. Additionally, it will provide understanding regarding the factors that influence the fiber constraint effect, modeling of the interphase region. A comparison of data obtained from 2D and 3D FE modeling will done to determine the best approach to be considered for other investigating other objectives.

- **Use AFM based force mapping to generate load–displacement curves near the fiber region of carbon fiber reinforced composites**: AFM indenters has a much sharper geometry that provides for a greater spatial resolution than conventional diamond-based tips used for instrumented indentation. For example, the effective cone half angle of a typical AFM tip is found to be approximately 10.69° while that for a Berkovich tip is 70.3°. Tranchida *et al.* [54] explained the ability of AFM indenter to evaluate the behavior of polymeric materials at smaller length scales than possible by depth sensing indentation techniques which use more blunt indenters. Munz *et al.* [35] have demonstrated that the interphase region in carbon fiber reinforced epoxy composites can vary between 20 to 80nm. However, Berkovich indenter creates an impression extending 6 to 9μm from initial contact point for an indentation

depth of 2μm.

- **Estimate the effect of fiber-constraint alone as a function of radial distance to the fiber**: Using a commercial Finite Element Analysis (FEA) tool, a model of the AFM indentation process in the near fiber region will be created. Major challenges such as modeling the complex shape of the AFM tip will also be addressed. The preliminary approach will be to use an elasto–plastic model for the matrix around the fiber. The carbon fiber will represented using a rigid boundary as it modulus value is two orders of magnitude higher than the matrix. The extent of impact of fiber–constraint on the modulus values will be used to as an indicator to evaluate whether there is a need for using inverse analysis technique or not.

- **Investigate the viscoelastic response of the interphase region and the impact of fiber constraint on the data collected near the fiber**: Polymeric materials exhibit time dependent behavior due to their unique molecular structure. The effect of the environmental conditions on polymers can be greatly influenced by the intrinsic viscoelastic behavior of the molecular structure of these polymers. Due to this reason, it is important to capture the true viscoelastic behavior of the matrix and interphase present in fiber reinforced polymer composites. Therefore, the approach used to evaluate the viscoelastic behavior along a radial line involves AFM indentation using a constant displacement of different hold periods. This will capture the stress relaxation of the interphase region as a function of the distance from the fiber. Based on the studies discussed previously about the effect of fiber constraint on the elastic modulus, it is reasonable to suggest that the measurement of the viscoelastic response of the interphase region can also be influenced by the fiber–constraint effect prevalent during indentation in the near fiber region. Hence, the material properties of the 3D FE model of the AFM indentation will be modified to incorporate a linear viscoelastic behavior using a generalized Maxwell model. A nonlinear elastic model will be used in conjunction with the linear viscoelastic definition of epoxy, taking

into account the limitations of FEA software available. This method will help to approximate the influence of the fiber–constraint on the viscoelastic response of the interphase region studied using the AFM indentation technique.

- **Evaluate the effect of UV irradiation on the elastic and viscoelastic response of the interphase region and bulk material using AFM indentation**: To demonstrate the usefulness of the force spectroscopy technique, the influence of environmental degradation such as exposure to UV irradiation will be considered. Exposure to UV rays can lead to degradation of the composites in terms of fiber, matrix and the interphase region [55–59]. Past research have provided information about the photo-catalytic degradation of the fiber and subsequent reactions by the free radicals [60]. This highlights the need to explore about changes in properties of the interphase region due to UV exposure. Carbon fiber reinforced epoxy composites exposed to UV radiation will be analyzed at nano-scale. Elasticand viscoelastic properties will be evaluated as function of two factors i. e. radial distance from the fiber and time period of UV exposure.

- **Study the effect of post curing and residual thermal stress on properties of the interphase region**: Carbon fiber and epoxy have coefficient of thermal expansion (CTE) that are very different–the fiber has a negative CTE in most cases and epoxy shows positive CTE [61]. This difference may have an important effect on the properties of the interphase and its width. Previous studies have computed the presence of residual stress due to thermal mismatch by various techniques [62–64]. Nonetheless, there is a lack of understanding on the impact of this contrasting behavior on the overall response of the interphase region. This work will investigate about the effect of post curing on the development of the interphase region and its elastic modulus. Additionally, the presence of residual stresses near the fiber on account of the thermal mismatch between the fiber and the matrix will be examined numerically.

CHAPTER 2

FINITE ELEMENT MODELING OF BERKOVICH NANOINDENTATION

2.1 Introduction

Commercial finite-element software ABAQUS v2016 (Dassault Systèmes, VÍizy-Villacoublay, France) was used to model and simulate diamond-tip nanoindentation. The objective of Finite Element Analysis (FEA) discussed in this chapter is to understand the difference between 2D and 3D FE modeling on the determination of the effect of fiber constraint. Additionally, this step is expected to help identify the factors to be considered while modeling the interphase region.

2.2 2D finite element model of Berkovich nanoindentation–Hardiman *et al.* [1]

2.2.1 Model development

Nanoindentation using a Berkovich indenter was simulated to understand the study done previously by Hardiman *et al.* [1]. Figure 2.1 shows the 2D axisymmetric model representing nanoindentation using a Berkovich indenter. The total number of nodes and elements were 1270 and 1188, respectively. Berkovich indenter was modeled as an axisymmetric rigid part, treating it as a cone with half angle of 70.3°. It provided a simplified representation with the same projected area to depth ratio as the full model of Berkovich indenter. Specimen was defined with material properties such as modulus value of 3.63 GPa and Poisson ratio of 0.34. Mohr–Coulomb yield criterion was used to specify the plastic behavior of the material. Friction angle and cohesion stress was specified as 26° and 82 MPa, respectively. The test was conducted as displacement controlled and indenter was

allowed to indent up to a depth of 1μm. Displacements perpendicular to the left side surface and bottom surface, respectively were set as zero. The fiber was represented by an encastre boundary to the right of the point of indentation, similar to the work seen in literature [1, 45, 49]. 4-node bilinear axisymmetric quadrilateral, CAX4 elements were used to mesh the specimen. A refined mesh was used near the point of indentation to capture the increased amount of deformation in that region. It was made coarser further away from the contact point between indenter and specimen using edge bias to reduce computational costs. Dimensions of the specimens in both directions were specified to be 300 times more than indentation depth, to avoid any far-field effects. Tests were conducted using standard model with loading and unloading steps specified as static general and NLGEOM turned on to account for the nonlinearities in deformations.

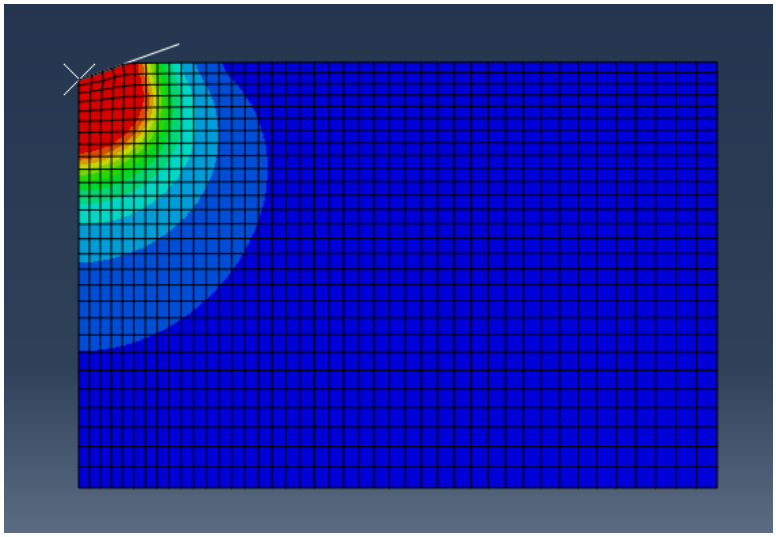

Figure 2.1: 2D model of nanoindentation using Berkovich indenter.

2.2.2 Elastic modulus evaluated by 2D model

The elastic modulus obtained from the 2D model closely matched with values indicated by Hardiman *et al.* [1](Fig. 2.2). It was observed that as the indents approached the fiber, there was an increase in modulus values. In FEA simulation, we know that only the influence of fiber bias is highlighted and any material property deviations in the interphase region that

may exist are not considered. The effect of fiber bias is evident from about $50\mu m$ away from the fiber.

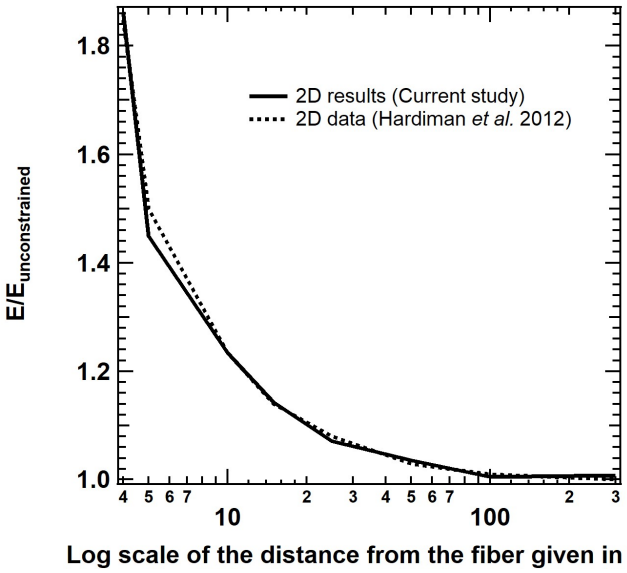

Figure 2.2: Comparison of modulus values from 2D model with data obtained from Hardiman *et al.* [1]

2.3 3D finite element model of Berkovich nanoindentation

2.3.1 Model developed by Hardiman *et al.* [1]

The 3D representation of Berkovich nanoindentation was done using the model exactly as setup by Hardiman *et al.* [1]. Berkovich indenter due to its symmetry was represented by a rigid plane at an angle of 24.7° from the surface of the specimen as illustrated in the Fig. 2.3. However during the simulation, it failed to achieve convergence due to severe distortion of elements. Even discussions with the authors failed to resolve the issue and replicate the study.

2.3.2 Full 3D representation of Berkovich nanoindentation

In order to address the challenges, a full representation of the Berkovich indenter, as shown in Fig. 2.4, was developed using the angles specified by a leading manufacturer, Micro

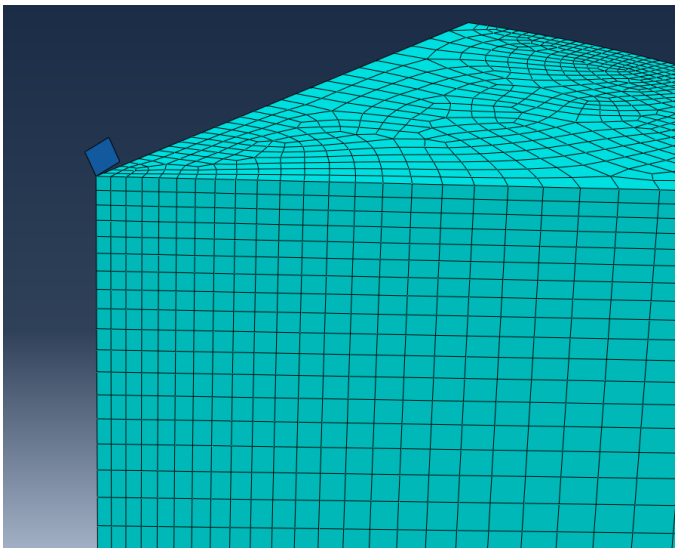

Figure 2.3: 3D model based on the specifications given by Hardiman *et al.* [1]

Star Tech, Huntesville, TX. and modeled as discrete rigid due to the complexities in its geometry. The properties for bulk material was specified similar to the 2D simulation. Specimen was modeled in two parts, one as an insert of fine mesh with 10μm length in x and z directions and a supporting structure of dimensions 300 times the indentation depth, with a coarse mesh. Both the parts were connected using a tie constraint. It was done to reduce computation cost and for obtaining finer mesh near the point of indentation. The aspect ratio of the elements in the insert were biased in the direction of indentation to reduce the amount of element distortion during simulation. Fiber was represented in the model by assigning the right surface of the specimen as a rigid constraint. The 8 node brick element (C3D8R) was used to model the specimen, as shown in Fig. 2.5. The total number of nodes and elements were 2276 and 1464, respectively. The indenter was allowed to indent up to a depth of 1μm and thereafter unloaded back to its original position. Standard model was used for the simulation, with loading and unloading steps specified as static general and NLGEOM turned on to allow the nonlinearities in deformations. The distance between the point of indentation and the rigid boundary was varied to understand the influence of the presence of fiber on indentation. In this study, a complete model of the indenter was used, whereas Hardiman *et al.* [1] had used a plane at 24.7° with the top surface of specimen to

represent it. The mesh distortion and convergence issue encountered in the former case was resolved with the use of complete model of the indenter, as there was more surface contact between the different parts and also it reduced the sudden collapse of elements just below the indenter tip.

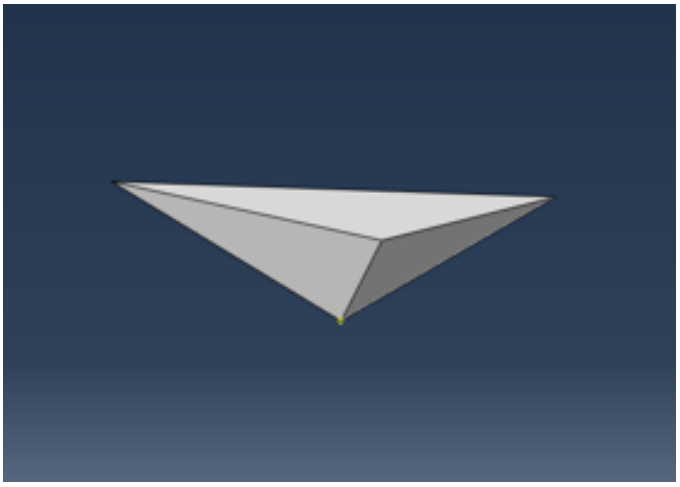

Figure 2.4: 3D model of Berkovich indenter

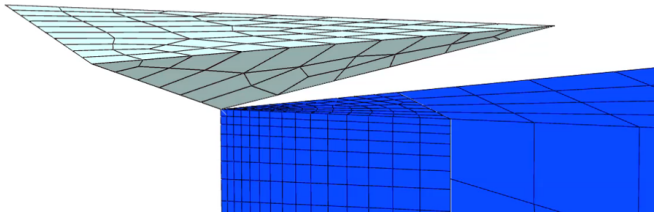

Figure 2.5: 3D model of nanoindentation using Berkovich indenter.

2.3.3 Elastic modulus evaluated by 3D model

3D simulation of Berkovich indentation was carried out to understand the deviations from 2D model. The elastic modulus values showed the same trend as in 2D simulation and is lower than 2D results due to more realistic representation, as shown in Fig. 2.6. The variation in the 2D and 3D model used in this study is given in table 2.1. There is a slight

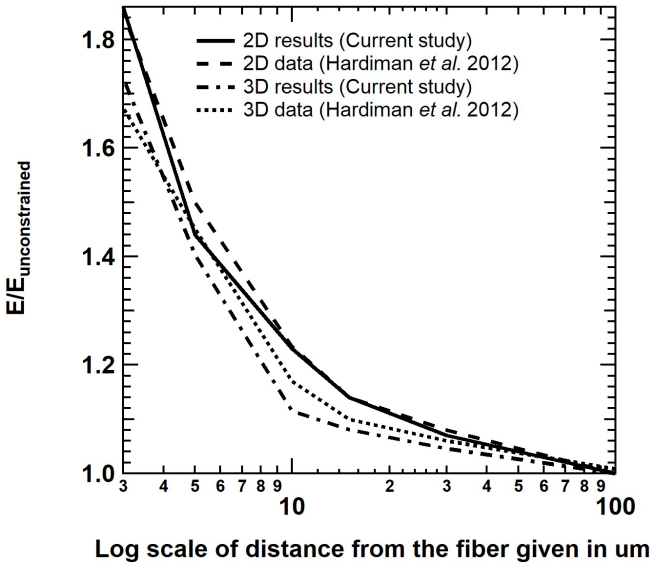

Figure 2.6: 2D and 3D simulation results compared to the 3D analysis by Hardiman *et al.* [1]

Table 2.1: Variation in the modulus values obtained using 2D and 3D models as a function of distance from fiber.

Distance from fiber (μm)	Normalized modulus values		Change (%)
	2D model	3D model	
100	1.00	1.00	-0.5
30	1.06	1.04	-2.0
15	1.13	1.08	-4.6
10	1.22	1.11	-9.9
5	1.85	1.40	-32.1
3	1.93	1.72	-12.2

deviation from the values indicated by Hardiman *et al.* [1] for 3D simulation. It can be attributed to the full representation of the Berkovich tip used in this study, compared to the rigid plane based on symmetry used by Hardiman *et al.* [1]. The modulus value of the bulk material was found to be 3.68 GPa by indenting about 100μm away from the fiber. Hardiman *et al.* [1] reported the elastic modulus of matrix as 3.70 GPa using 3D model. Table 2.2 gives the percentage change in results obtained by Hardiman *et al.* [1] and the 3D model representing complete geometry of Berkovich indenter.

It can be observed that fiber bias is influenced by the geometry of the indenter. Full rep-

Table 2.2: Variation in the modulus values obtained using 3D model and Hardiman *et al.* [1] as a function of distance from fiber.

Distance from fiber (μm)	Normalized modulus values		Change (%)
	Hardiman *et al.* [1]	3D model	
100	1.00	1.00	-0.5
30	1.06	1.04	-1.9
15	1.10	1.08	-1.9
10	1.17	1.11	-5.4
5	1.47	1.40	-5.3
3	1.67	1.72	2.9

resentation of the Berkovich indenter has led to rise in fiber bias effect due to the increased amount of contact with the fiber. The interaction of the stress field with the rigid boundary representing the fiber is shown in Fig. 2.7. From the FEA simulation results, the impact that fiber bias on the elastic modulus in the interphase region is confirmed.

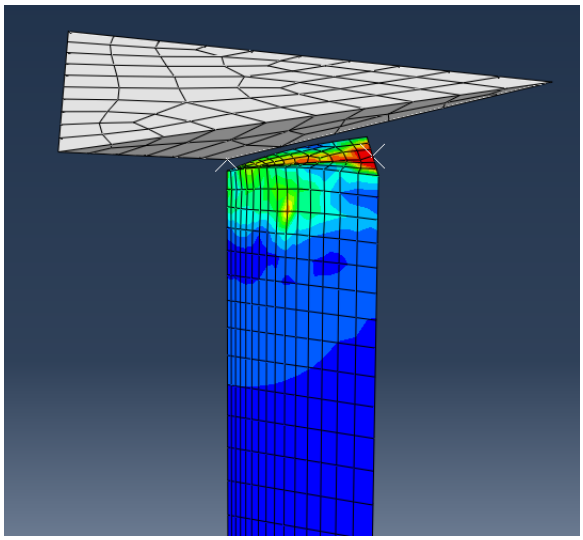

Figure 2.7: Interaction of stress field due to indentation with the rigid fiber.

2.4 Conclusion

As a preliminary step, the influence of fiber bias was verified with reference to the work done by Hardiman *et al.* [1]. The 2D simulation of Berkovich nanoindentation closely matched the results given in literature. Elasto-plastic material properties were assumed and

Oliver–Pharr method was used to evaluate the properties to replicate the methodology used by Hardiman *et al.* [1]. Attempts to replicate the 3D simulation work failed due to convergence issues. In order to circumvent the issue, a full representation of the Berkovich tip was developed. The elastic modulus values obtained from 3D simulations were closer to the true properties of the bulk material than 2D simulation. This indicated that 3D representation is essential to capture the indentation process entirely. A complete representation of the Berkovich nanoindeter is required for preventing excessive distortion of elements below the point of indentation. It is understood that to study the concept of fiber constraint, the assumption of axisymmetry must be ignored as it will typify a circular matrix pocket with presence of rigid boundary around it. This will be discussed further with regard to FE modeling of AFM indentation.

CHAPTER 3

AFM INDENTATION

3.1 Introduction

Evaluation of the fiber bias effect have been confined to the use of Berkovich indenter as seen from the literature [1, 48, 49]. It is estimated that the width of the interphase region in the carbon fiber reinforced polymer is in the range of 50 nm to 300 nm. Therefore it can be understood that AFM indenters due its high spatial resolution when compared to Berkovich indenter, provides a good tool to study the interphase properties very close to the fiber.

As discussed previously, in the interphase region the presence of fiber which can be considered as a rigid boundary due to its high stiffness needs to be considered as it will provide an apparent increase in the modulus value due to the fiber constraint. This occurs due to the reflection of stress fields from the rigid boundary. In turn, it may mask the true behavior of the interphase properties that can be determined using indentation technique. Hence, there is a need for quantifying the influence of fiber constraint on the evaluation of mechanical properties of the interphase region. A numerical approach is also considered to study this effect on the properties of the interphase in fiber reinforced polymer composites.

3.2 AFM indentation - Experiment

3.2.1 Material preparation

In this study, interphase samples were prepared by embedding carbon fibers in an epoxy matrix. Carbon fiber tows with 6k filament count was obtained from Hexcel (Stamford, CT, USA). Selected fiber was already surface treated by Hexcel before acquiring. The poly-

mer matrix was prepared using a diglycidyl ether of bisphenol–F (DGEBF) based epoxy resin (EPON 862®) (Fig. 3.1), cured using an aliphatic amine based hardener (EPIKURE 3274®). Both epoxy and hardener were acquired from the Miller-Stephenson Chemical Company (Dunbury, Connecticut, USA). Curing was done at room temperature for 24 hours and post-curing at 121°C for 6 hours.

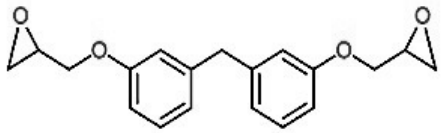

Figure 3.1: Chemical structure of DGEBF.

Small circular blocks of samples were cut using precision cutter (ISOMET 1000, Buheler, Lake Bluff, Illinois) and polished using metallographic techniques starting from 320 grit grinding paper to 0.05 μm alumina particles using an automated polisher (Labopol 5, Struers, Cleveland, Ohio, USA). Initially sample preparation was done by cryo-microtoming using a diamond knife, however, it was found that the epoxy smeared over the carbon fiber and it was difficult for to obtain clear images of the surface. SEM images of surfaces obtained after cryo-microtiming and mechanical polishing are shown in Fig. 3.2, respectively. Therefore, it was avoided for other sample preparations. The RMS value of surface roughness after polishing was found to be approximately 4 nm, using AFM imaging technique. The indentation depths need to be greater than the surface roughness in order to avoid the influence of surface artifacts on the data collected.

3.2.2 Generation of elastic modulus maps using AFM indentation

An atomic force microscope (MFP–3D, Asylum Research, Santa Barbara, CA, USA) was used for performing AFM indentations on the prepared samples. The AC160TS AFM indenter tip, manufactured by Olympus Micro Probes (Center Valley, PA, USA), which is recommended for study of polymers, was employed. It has a resonant frequency in air of

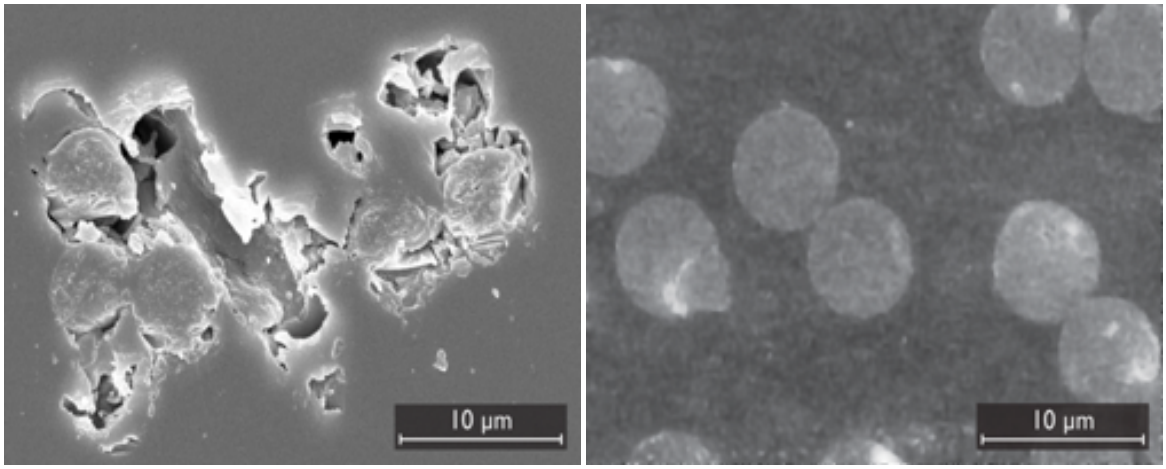

(a) Cryo-microtomed (b) Mechanically polished

Figure 3.2: SEM images of the sample.

300kHz (100 - 400 kHz) and a typical spring constant of 26 N/m (8.4 to 57 N/m). Figure 3.3 shows the topographical images of the carbon fiber obtained from the scanning area in tapping mode. The initial scan size was set at 65 μm to capture the set of carbon fibers embedded in the matrix and thereafter each scan involved a zoom for obtaining a closer image of the carbon fiber. The final image size was approximately 1μm that contained a portion of the carbon fiber, the matrix and the interphase region. In this regard, it is good to note that the average diameter of a carbon fiber filament in a tow is about 5 to 10 μm. The height profile of the carbon fiber shown in Fig. 3.4 indicates a dip on the top of the fiber, this may be due to the oxidation of carbon fiber during mechanical grinding or polishing.

Prior to force spectroscopy, calibration of the AFM cantilever was done to determine the spring constant and inverse optical lever sensitivity (InvOLS). Sader method [65], which was incorporated in the software was utilized to estimate the two parameters. The spring constant and InvOLS were observed to be about 42 N/m and 56 nm/V, respectively. Using the contact mode, force maps were generated at each point covered with 48 by 48 grid across a square region of 950 nm $\times$ 950 nm. All the force maps were done as load controlled.

In order to obtain meaningful interpretation of the collected data, a MATLAB code was written (Refer Appendix). Key objective of this step was to capture data along radial lines

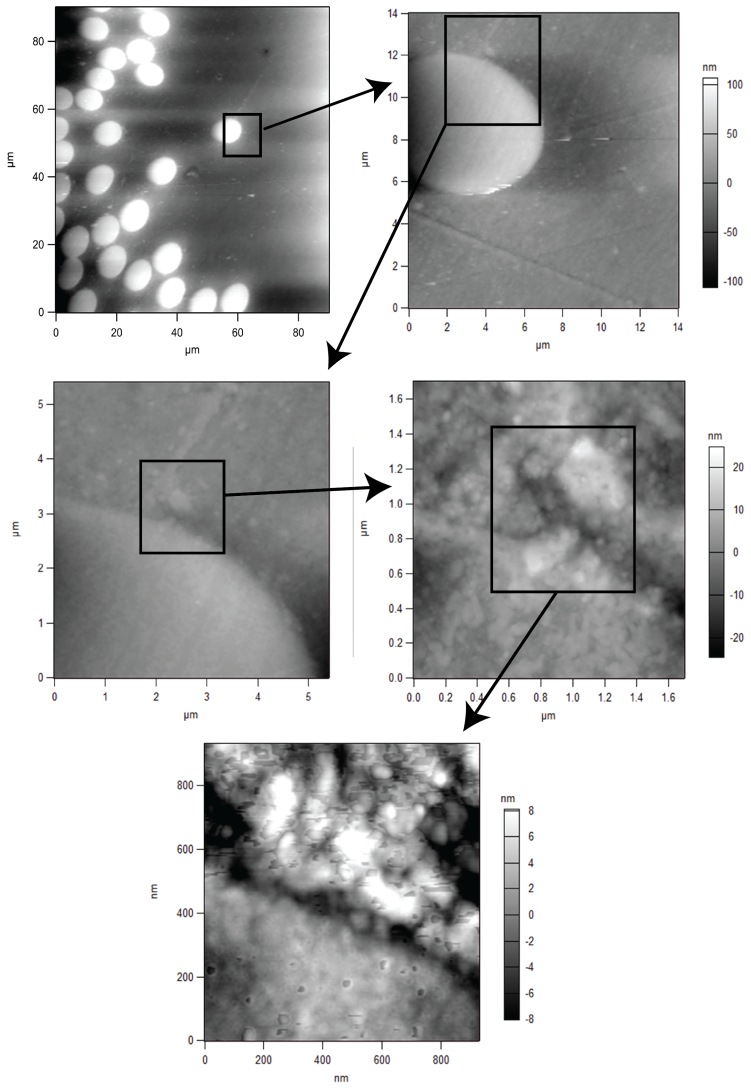

Figure 3.3: Topographical images of carbon fiber reinforced polymer.

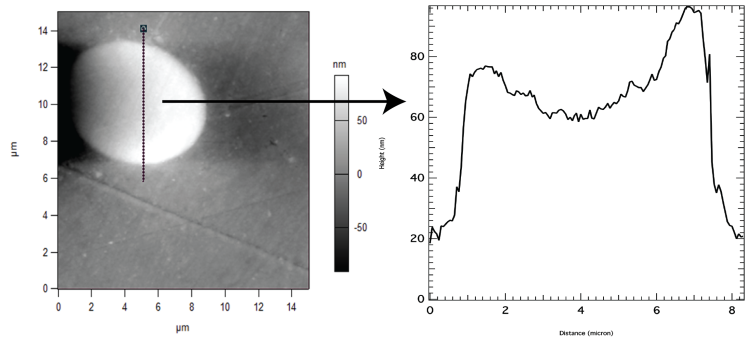

Figure 3.4: Height profile of carbon fiber.

from the boundary of the fiber. As described previously, adhesion map was used to identify the points on the modulus map corresponding to the boundary of the fiber and it was given as input to the MATLAB code in the form of coordinates. Using basic mathematical equations of circle, a portion of circle was superposed over the boundary of the fiber and the center of the corresponding circle was determined. Equation of radial line was then employed to form radial lines from the boundary of the fiber. Coordinates of points lying along each radial line was obtained as the output of the code. This was later used to extract load–displacement curves from the AFM for the respective points.

3.3 FEA modeling of AFM indentation

Commercial finite-element software ABAQUS v2016 (Dassault Systèmes, VÍizy-Villacoublay, France) was used to model and simulate AFM based indentation of the interphase region in the 3D space, given in Fig. 3.10.

3.3.1 AFM indenter model

Few of the dimensions needed for modeling of the tip were collected from the website of the manufacturer, Olympus Micro Probes (Center Valley, PA, USA). However it was recommended by Asylum Research, Santa Barbara, CA, USA to perform Scanning Electron Microscope (SEM) imaging of the AFM indenter AC160TS to obtain closer look at tip geometry. SEM images of the AFM indenter at different length scales are given in Fig. 3.5. Figures 3.5 (c) and (d) were provided by the manufacturer of the tip. Considering the maximum indentation depth of 27 nm observed in this study, geometric dimensions of the indenter up to a height of 1000 nm from the tip were collected. The front angle of the tip is 0° and back angle is 35°. As noted previously, the tip was observed to be rounded with a radius of about 10 to 15 nm. The 3D model of the AFM tip was created as shown in Fig. 3.6. The AFM indenter was modeled as discrete rigid due to complex geometry with a tip radius of 15 nm, as its elastic modulus is very high as compared to the specimen and

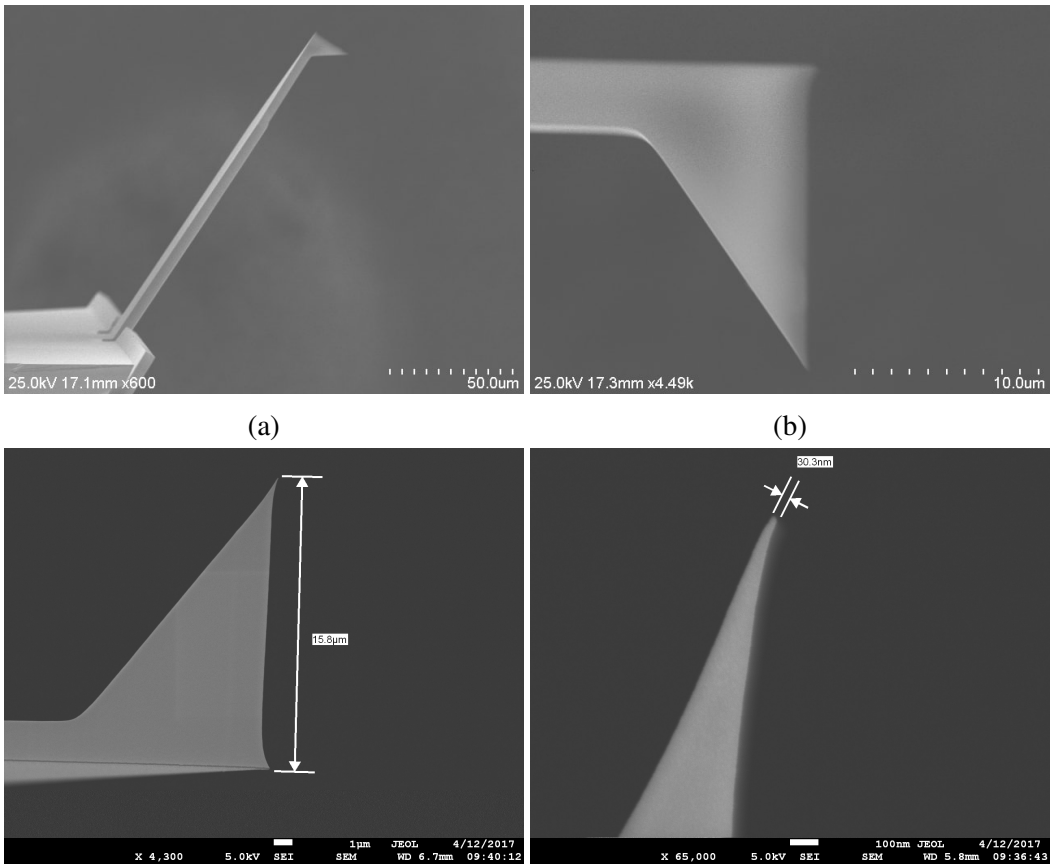

Figure 3.5: SEM images of the AFM indenter at different length scales.

its degrees of freedom were constrained in the directions perpendicular to the loading.

Determination of area function of the AFM indenter

To accurately evaluate the mechanical properties of the sample being probed by the AFM indenter, it is essential to determine the area function of the AFM indenter used. The general contact area A_c of an indenter is given by the Eq. (3.1).

$$A_c = C * {h_{in}}^2 \tag{3.1}$$

where, C is a constant dependent on the indenter geometry and h_{in} is the indentation depth. The area function of Berkovich indenter is very well-known and widely used as $A_c = 24.5 * h^2$. However, it is not trivial to determine the value of C for an AFM indenter

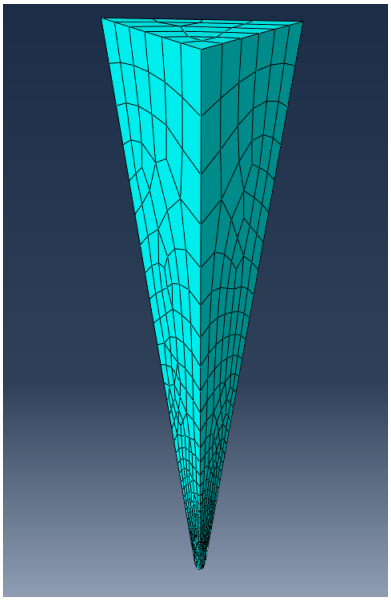

Figure 3.6: 3D model representing AFM indenter.

from its geometry due to its complex tip geometry and its positioning on the cantilever. Therefore the FEA model of the AFM indenter developed in the previous section with the aid of SEM images of the tip will be employed to evaluate the value of the constant, C. The AFM manufacturer of the indenter used in this study, Asylum Research (Santa Barbara, CA, USA) had indicated that the AFM tip indents at an angle of 10° with the specimen, so the indenter tip was tilted at 10° with the vertical axis for the evaluation of the area function. Various partition planes normal to the vertical axis were placed along the height of the indenter. The indenter shape resulted in a triangular intercept of varying size on the partition plane as a function of the height of the indenter. Lengths of these triangular intercepts were measured for indentation depths ranging from 0 nm to 960 nm. Area of these triangular intercepts whose sides have lengths a, b and c were then calculated using the well known Heron's formula given in Eq. (3.2). The plot of the area function to the indentation depth is given in Fig. 3.7.

$$A = \sqrt{s*(s-a)*(s-b)*(s-c)} \tag{3.2}$$

where, s is the semiperimeter of the triangle, $s = \frac{(a+b+c)}{2}$

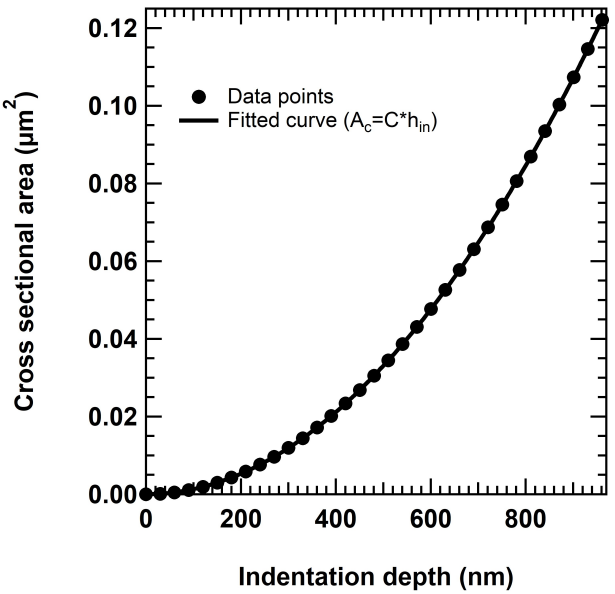

Figure 3.7: Cross section area of the AFM indenter AC160TS versus the indentation depth.

The general relation given in Eq. (3.1) was used to fit the data and thereby determine the value of C. It was determined that the area function of the AFM indenter used in this study is given by, $A_c = 0.1321 * h_{in}^2$, where h_{in} is the indentation depth in nanometers.

3.3.2 Axisymmetric modeling of the interphase region

An axisymmetric model is generally considered for the modeling of the interphase region [1,66]. However, this assumption considers the interphase region as a cylinder shaped matrix region surrounded by the rigid boundary representing the fiber, which doesn't denote the real case. Such a case can be expected to overestimate the effect of fiber constraint on the properties determined in the region near the fiber. In this study, an axisymmetric model and a realistic representation of AFM indentation near the fiber is studied to accurately estimate the effect of fiber constraint on the properties of the interphase region.

A simplified 2D axi–symmetric model of the AFM indentation was initially considered to simulate the force mapping on CFRP. Based on same projected area to depth ratio

concept, the equivalent cone angle of the AFM tip AC160TS was evaluated using its geometry as 10.69°. Similar to the Berkovich nanoindentation described previously, the indenter could be modeled as a line representing the side of the equivalent cone at an angle of 10.7°, as shown in Fig. 3.8. However as the indenter was modeled as very sharp, it will fail to establish any contact with the substrate. But most importantly, it was realized that a axi–symmetric model (3D axisymmetric model given in Fig. 3.9) is not a good representation of the problem to study the fiber bias effect.

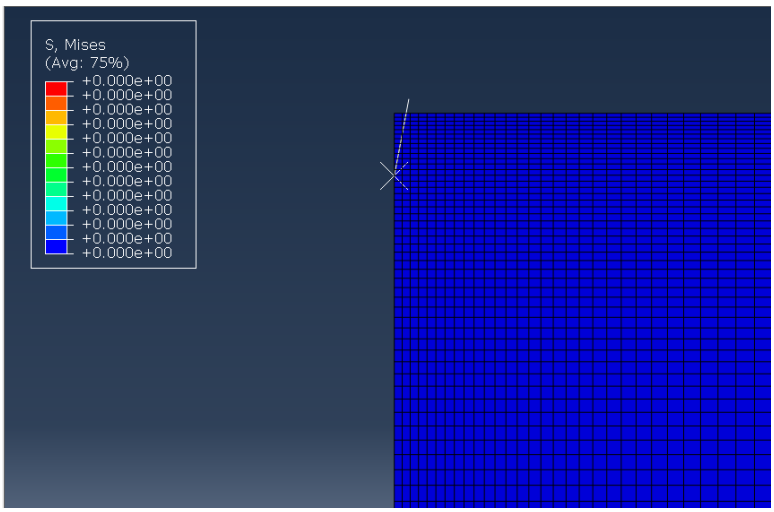

Figure 3.8: AFM indenter modeled using effective cone angle.

To reduce computational cost and to provide finer mesh at the point of indentation, specimen was modeled as two parts using 8 node brick element with reduced integration elements (C3D8R) with minimum element size of 1 nm. The first part was modeled as a deformable wedge shaped insert of 60° and 50 nm length with extra fine mesh, as large local deformation takes place in this region. The other part was a supporting wedge shaped structure of coarse mesh with all the dimensions set as 300 times the maximum observed indentation depth, to ensure far field effects were negligible. A tie constraint was used to connect the two parts. Figure 3.9 shows the 3D axi–symmetric FE model representing the AFM indentation. As noted previously, the indenter tip was placed at 10° with the top surface of the specimen.

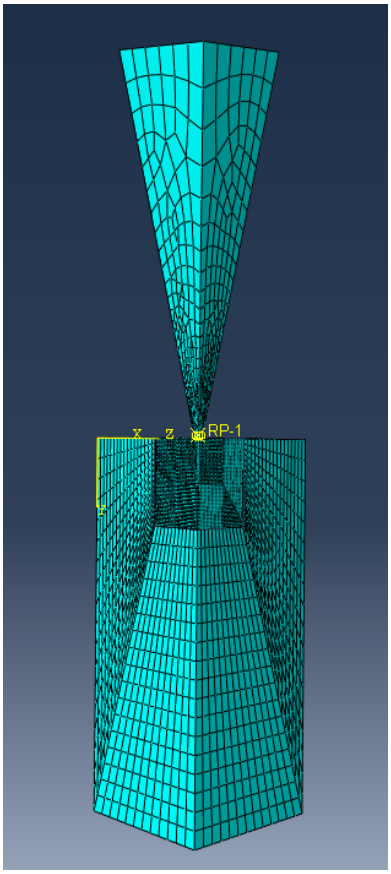

Figure 3.9: 3D model representing AFM indentation.

Displacement controlled indentations were done in 3D space to minimize instabilities in the simulations. Frictionless contact was assumed between the indenter and the specimen. A 4-node 3-D bilinear rigid quadrilateral element (R3D4) was used to mesh the indenter. Encastre boundary condition was specified to right–hand end of the specimen to represent the rigid fiber constraint. A roller boundary condition was applied to the bottom region of the specimen. Additionally, the degree of freedom perpendicular to the sides of the specimen were constrained to remove instabilities. Surface to surface interaction was defined between the indenter (master) and the top surface of the specimen (slave). Loading and unloading for the simulation were defined as independent static general steps. The NLGEOM option was used to account for the nonlinearities present in the deformation. The reaction force (RF) at the reference point (RP) of the indenter, along the axis of loading was collected as the load data. The displacement in the direction of loading of the left top corner node of the wedge shaped specimen i.e. just beneath the indenter tip was recorded as the displacement data.

Simulations were done at different distances from fiber, denoted by r in Fig. 1.3 to determine the impact of fiber constraint on the measured properties of the near fiber region. The values of r were selected keeping in view of the resolution of modulus map obtained experimentally and included values: 600nm, 400nm, 200nm, 100nm, 60nm, 40nm and 20nm. Average of indentation depths at the different value of r observed in experiments were used for the simulations.

3.3.3 Realistic representation of the interphase region

The impact of fiber constraint alone is captured using the FE analysis as the variation in material properties of the interphase is ignored and the substrate is assumed to be a block with uniform properties defined by elastic and plastic properties. Material properties of the substrate, mesh elements of the substrate as well as the minimum size were defined in the same way as the finite element modeling done in the case of the axisymmetric model shown

in Fig. 3.9. A curved region of radius 2.5 μm was carved out of one end of the block to represent the rigid contour of the carbon fiber boundary. The AFM indenter was modeled as discrete rigid, in similar manner as the modeling done in the axi–symmetric case [66].

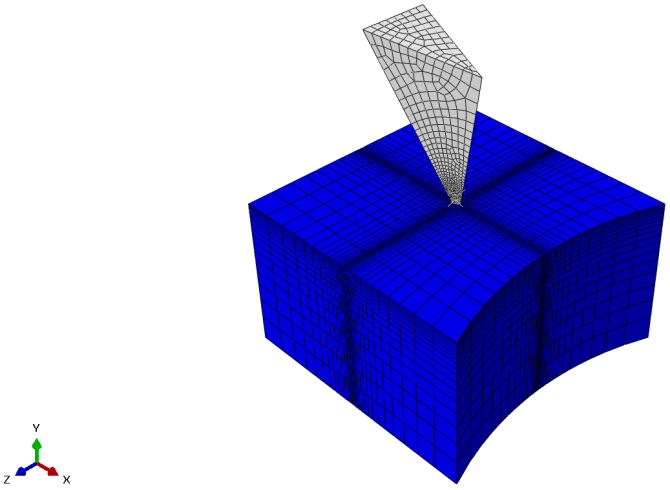

Figure 3.10: Modified 3D model representing AFM indentation.

Two boundary conditions were used for the substrate. The first one was a roller boundary condition applied to the bottom region of the specimen and the other one was an encastre boundary on the curved surface representing the boundary of the fiber. All the degree of freedom except the y-direction were constrained for the indenter using a displacement based boundary condition. The interaction between the indenter (master) and the top surface of the substrate (slave) was defined as surface to surface. Loading and unloading were carried out as a single static general step using a displacement based boundary condition with defined amplitude. The NLGEOM option was used to account for the nonlinearities present in the deformation of the substrate.

Simulations were done at different distances from fiber, denoted by r to determine the impact of fiber constraint on the measured properties of the near fiber region. The different values of r were selected keeping in view of the resolution of modulus map obtained experimentally. Average of indentation depths at the different value of r observed in experiments were used for the simulations [66]. For this reason, the substrate was partitioned at the dif-

ferent values r for the respective simulations, as shown in Fig. 3.10. The reaction force (RF) along the axis of loading at the reference point (RP) of the indenter was recorded as the load data. The displacement in the direction of loading of the node at the intersection of the partition was collected as the displacement data.

3.4 Conclusion

The experimental portion of this study consisted of load controlled force spectroscopy using AFM indenter on a region of approximately $1\mu m$ comprising of the carbon fiber and the near-by epoxy. The depth of penetration decreased from approximately 25 nm to 5 nm as the distance from fiber was varied from 600 nm to 20 nm, for the same maximum load of 870 nN. The adhesion map was used to identify the contour of the fiber and was used in a MATLAB code that was developed to extract modulus values along radial lines to the fiber.

A FE model of the AFM indenter used in the experiments was developed to numerically study the indentation of the interphase region. Additionally, the FE model of the indenter was used to find the area function of the indenter i.e. a relationship between the area of contact during the indent and the corresponding indentation depth. A modified finite element model of the interphase region is created to obtain a realistic representation of the AFM indentation in the interphase region in the fiber reinforced polymer composites. This model overcomes the drawback of previous studies which have considered models of interphase region as a circular matrix pocket surrounded by the fiber, due to the assumption of axisymmetry. Additionally, this model will offer an accurate estimation of the effect of fiber constraint on the properties of the near-fiber region. The specimen was modeled as a block in 3D space with a curved surface at one end of radius 2.5 μm, representing the rigid fiber.

CHAPTER 4

ELASTIC BEHAVIOR OF INTERPHASE REGION

4.1 Introduction

The results from the experimental and numerical approaches using AFM described in chapter 3 are analyzed in this chapter in terms of the elastic properties. A careful examination of the changes in the elastic modulus along a radial line to the carbon fiber is done to determine the variations in the interphase behavior. Furthermore, the influence of fiber constraint on the evaluation of interphase properties is determined using Finite Element Analysis (FEA).

4.2 Elastic modulus maps generated using AFM indentation

Force mapping technique using AFM was conducted as load controlled indentations with maximum load of 870 nN. The maximum observed indentation depth was 27 nm. Figure 4.1a shows the modulus map generated by 'full field' force displacement curves. Every point on the modulus map uniquely represents the elastic modulus obtained from each of the 2304 load–displacement curves. The modulus values were generated using the in–built tool based on Oliver–Pharr method [34]. It was difficult to precisely distinguish the contour of the carbon fiber using the modulus map. Therefore adhesion map shown in Fig. 4.1b was used to estimate the contour of the carbon fiber. It can be observed that the adhesion of the tip is higher on the epoxy than the carbon fiber; making it possible to determine the position of the fiber boundary in the image with ease. It can be observed using the color scheme that the modulus of carbon fiber is shown as 15 GPa, which is significantly lower than its nominal value. This can be attributed to the limitation of the AFM tip used. It is important

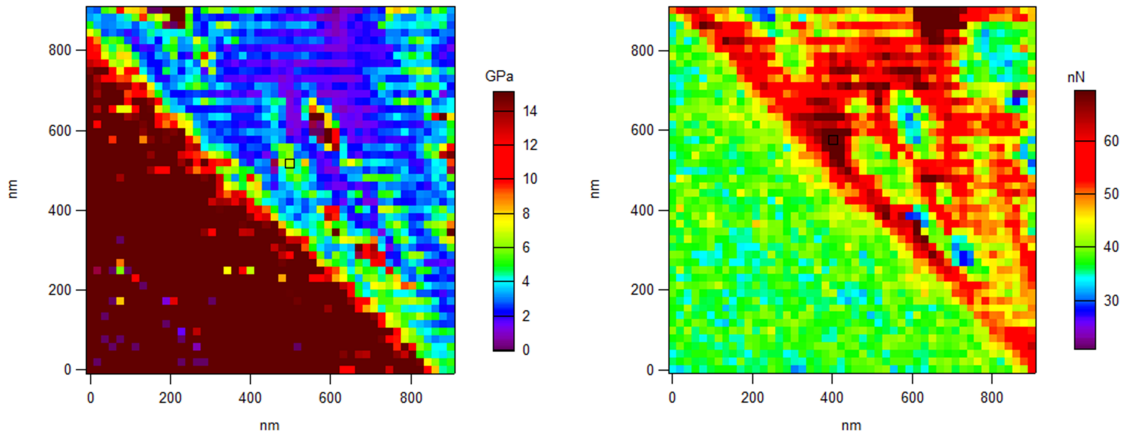

(a) Modulus map (b) Adhesion map

Figure 4.1: AFM plots of interphase region in carbon fiber reinforced epoxy.

to note that we are able to obtain the load–displacement data for each indent across the 48 by 48 grid. The load–displacement curves obtained in the bulk material will be used to validate the FEA simulation of AFM indentation.

In order to remove the ripples in the data due to noise from feedback loop and other electrical signals of the equipment, Fast Fourier Transform was done on the load-displacement curve to determine the frequency of the data. A low pass filter (LPF) was then used to remove the noise and extract the true data. Figure 4.2 shows the filtered curve along with the actual load-displacement data collected from the AFM.

To process the data obtained from force mapping, previously discussed MATLAB code was employed and the load–displacement curves obtained were studied as a function of the radial distance to the fiber (Fig. 4.3a). It can be noted that there is a 'shift' in the load–displacement curves as the indentation was done closer to the fiber. Similar observation can be made in Fig. 4.3b, which shows that the maximum indentation depth was reduced considerably while indenting closer to the fiber, for the same maximum indentation load. A gradient in the modulus while traversing from the carbon fiber to matrix can also be noted. The points lying on the fiber's boundary were identified using the adhesion map and was given as the input to the MATLAB code to superpose a circle over the boundary of the fiber. Equation of tangent line was then employed to form radial lines and thereby extract

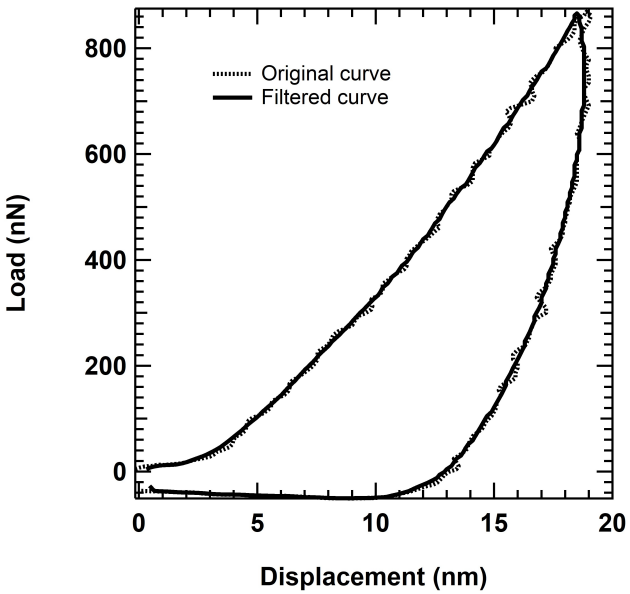

Figure 4.2: Filtered load-displacement curve and data obtained from AFM.

the modulus values from the matrix along the radial lines. Each pixel in the grid denotes an approximate distance of 20 nm. Figure 4.4 shows average elastic modulus values of 20 radial lines that were plotted as a function of the distance from fiber. An exponential curve was used to fit the change in modulus values along the radial lines from the boundary of the fiber. Based on the change in elastic modulus values, the width of the interphase region was determined to be approximately 250 nm. As noted previously, the increase in elastic modulus of the interphase determined by indentation technique can be a combination of the variation in material properties of the region and the influence of fiber constraint.

It can be observed from figure 4.4 that the error bars for average modulus values away from the fiber are very small compared to those near the fiber. This can be attributed to the fact that the indentation depths are much higher for force mapping done in region away from the fiber than the indents carried our closer to the fiber. In addition, the influence of surface roughness becomes more evident at shallow indentation depths, leading to significant variability. But as shown in figure 4.4, the existence of variation in modulus along the radial line can be confirmed, taking into confidence the span of error bars. However as discussed previously, it is important to distinguish the apparent rise in modulus due to fiber

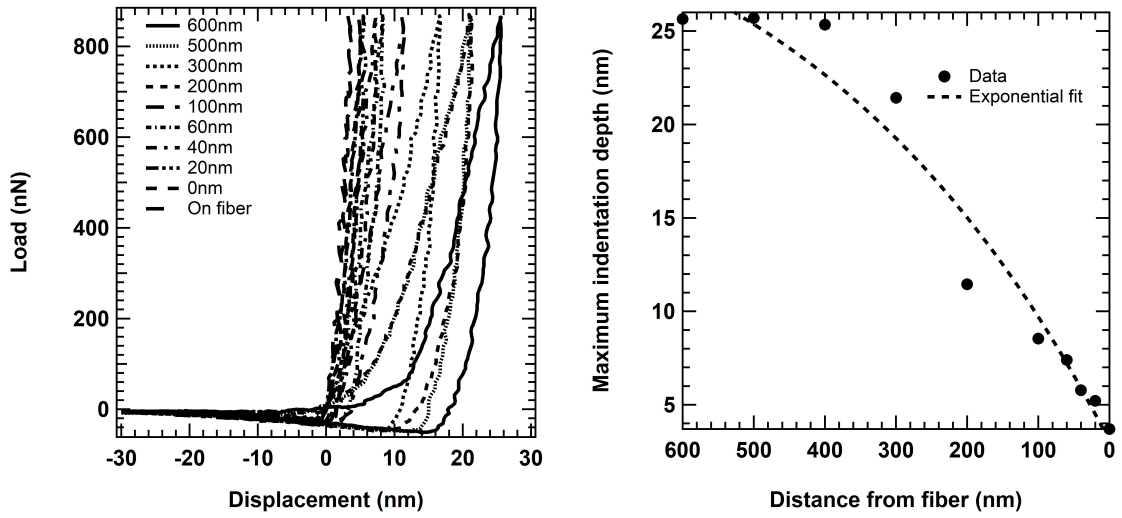

(a) Load–displacement curves along a radial line to the fiber.

(b) Maximum indentation depth vs radial distance to the fiber for constant indentation load.

Figure 4.3: Extracted AFM indentation force map data.

constraint because accurate determination of interphase properties will provide precise assessment of the performance of the composite structure.

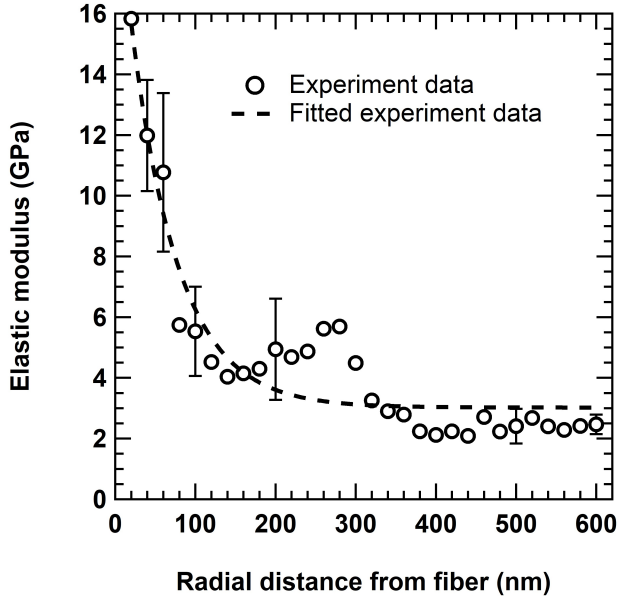

Figure 4.4: Average variation of the elastic modulus evaluated from experiment along with exponential fitted curve as a function of distance from the fiber.

4.3 Impact of fiber–constraint on elastic modulus of near–fiber region

4.3.1 Modeling elasto–plastic behavior of epoxy

The preliminary approach was to model epoxy as a purely elastic material using the elastic modulus value and Poisson's ratio. Experimental data was used to specify the elastic properties of the specimen as elastic modulus, E = 2.78 GPa and Poisson's ratio, ν = 0.34. However, the FE simulations of the elastic material model resulted in severe convergence issues after certain indentation depth. The distortion of the elements beneath the indenter tip indicated that it was due to a lack of sufficient material definition. In this regard, it is very important to note that due to the extreme sharpness of the AFM tip compared to the Berkovich tip, the amount of plasticity that occurs in the material below the tip is quite significant. Hence, it was essential to develop a suitable plastic model in addition to the above indicated elastic properties for the epoxy being used as the matrix. Plasticity was defined using the average yield strength determined as 92.7 MPa by compression tests carried out on epoxy samples according to ASTM standard D–695 [67]. For this test, cylindrical samples of 25.4 mm (1 in) height and 12.25 mm (0.5 in) diameter were prepared. Nominal stress–strain curve obtained for one of the samples is shown in fig. 4.5.

Isotropic hardening was used to model the hardening behavior of the specimen. Ramberg–Osgood model given in Eq. (4.1) was fitted to the compression test data to evaluate the yield offset, $\alpha\left(\frac{\sigma_0}{E}\right)$ and hardening exponent, n. Where, σ_0 refers to the yield stress and E denotes elastic modulus. Multiplier and exponent were evaluated as 0.0593 and 0.99, respectively.

$$\varepsilon = \frac{\sigma}{E} + \alpha\frac{\sigma}{E}\left(\frac{\sigma}{\sigma_0}\right)^{n-1} \tag{4.1}$$

4.3.2 Finite element analysis of the interphase properties

Fig. 4.6 shows the load–displacement curves obtained from 3D FEA model of AFM indentation. It can be observed that for the indents done on the same material, there is a

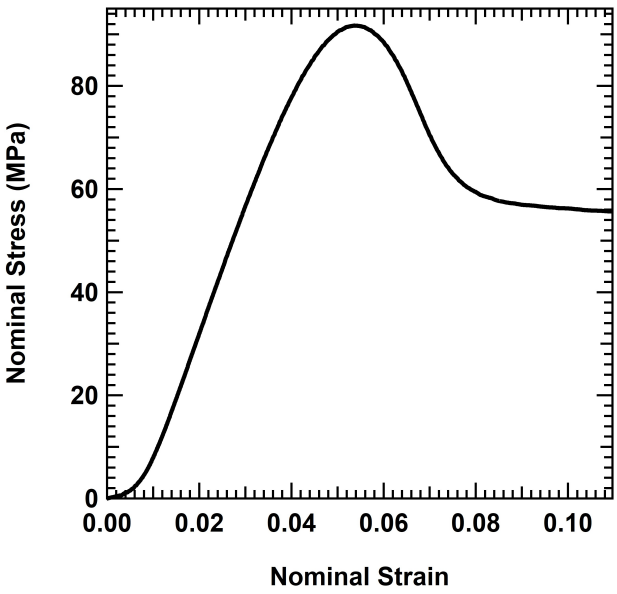

Figure 4.5: Nominal stress-strain curve for epoxy.

shift in the load–displacement curves for indents at 20 nm and 40 nm away from the fiber. This can be attributed to the stiffer response due to the interaction of indentation generated stress contours with the encastre boundary representing the rigid fiber, as shown in Fig. 4.7. The AFM indenter's shape and indentation depth are factors affecting the impact of fiber constraint on the evaluation of properties of the near-fiber region. Oliver–Pharr method [34] was used to evaluate the elastic modulus from the load–displacement curves at different distances from the fiber. The elastic modulus of the polymeric matrix - epoxy was determined from indentation at 600 nm away from the fiber as 2.76 GPa.

Figure 4.8 shows the comparison of elastic modulus evaluated from modulus maps, realistic FEA model of the AFM indentation in the interphase region and the results found using an axi–symmetric model [66]. It can be observed that the effect of fiber constraint in visible only within 40 nm away from the fiber. The realistic FEA model offers two unique perspectives compared to previous studies. One is that the boundary representing the fiber is not used based on axisymmetry assumption. Second, the influence of the curved boundary of the fiber on the fiber constraint effect is also captured in this data, unlike the axi–symmetric model. Additionally, these results also demonstrate for the first time

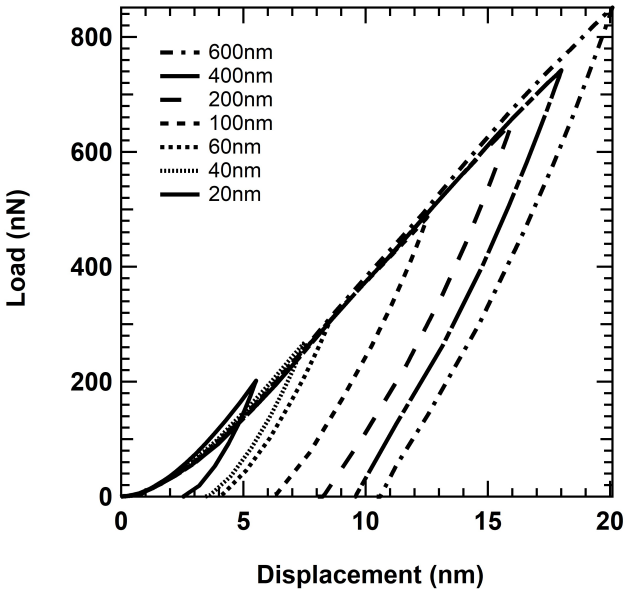

Figure 4.6: Load–displacement curves obtained using 3D finite element model of AFM indentation.

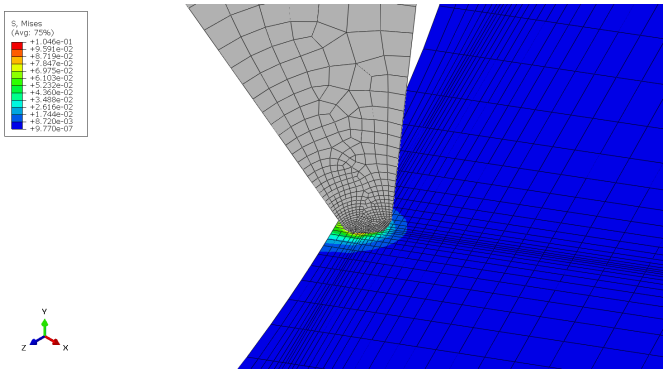

Figure 4.7: Interaction of stress fields with fiber while indenting close to the representative rigid constraint.

quantitatively that AFM indentation is not as affected by the fiber constraint as in the case of Berkovich indentation. This is due to the reason that the effective cone half-angle of the AFM indenter is very small compared to the Berkovich indenter.

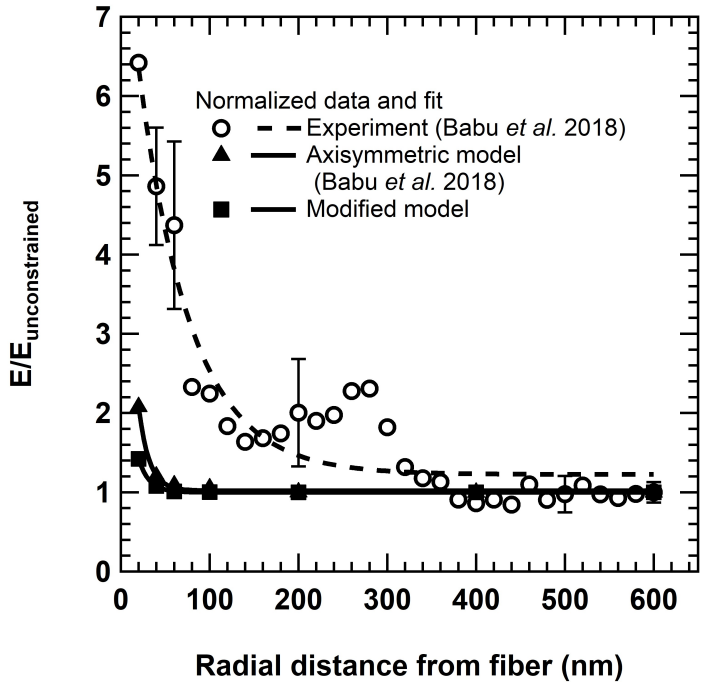

Figure 4.8: Comparison of elastic modulus evaluated from the modified model and axi–symmetric model.

It is important to note that the realistic model estimates the effect of fiber constraint to be about 32% lower than the value evaluated using the axisymmetric model. Also, the increase in modulus due to fiber constraint at 40 nm away from the fiber is found to be only 8%. This confirms that the use of an axisymmetric model of the interphase region in fiber reinforced composites leads to an overestimation in the evaluation of the impact of fiber constraint effect. Analysis of the data obtained from the realistic model with the experimental values is also done. It shows that the contribution of fiber constraint to the increase in modulus value in the interphase region is not very significant compared to the increase resulting from the interaction between matrix and fiber during the curing process, taking into confidence the length of the error bars. Hence, it confirms the mechanical properties of interphase region are distinct from the bulk matrix. Also, AFM based indentation is an effective tool to

evaluate the properties of small interphase regions with minimal impact of fiber constraint effect.

4.4 Conclusion

Data analysis of the modulus maps of the interphase region obtained using AFM indentation indicates that there is a gradient in the average elastic modulus values along a radial line to the boundary of the carbon fiber. Using this method the width of the interphase region in carbon fiber reinforced epoxy was approximated as 250 nm. The gradient in elastic modulus values can be attributed to the chemical interaction between the carbon fiber and the nearby epoxy or the influence of the fiber constraint effect due to the presence of the rigid fiber in the vicinity of the indent.

Two finite element models were considered to evaluate the effect of fiber constraint in the interphase region. First one assumed axi-symmetry and the second one is a realistic representation of the AFM indentation done in the interphase region of the fiber reinforced polymer composites. The realistic model overcomes the drawback of previous studies which have considered models of interphase region as a circular matrix pocket surrounded by the fiber, due to the assumption of axisymmetry. Additionally, it offers an accurate estimation of the effect of fiber constraint on the properties of the near-fiber region. The specimen was modeled as a block in 3D space with a curved surface at one end of radius 2.5 μm, representing the rigid fiber. Results of the 3D FE simulations carried out at varying distances to the fiber confirm that fiber constraint affects the evaluation of properties within 40 nm of radial distance from the fiber. It is noted that there is an apparent increase in elastic modulus of about 42% and 8% due to fiber constraint for indents at 20 nm and 40 nm away from the fiber, respectively. There is no effect of fiber constraint observed for indents done beyond 40 nm of radial distance from the fiber.

Comparison of the results from the modified model to the axisymmetric model shows that assumption of axisymmetry leads to an overestimation in fiber constraint by 32% for

indentation done at 20 nm away from the fiber. Most importantly, these results still confirm that effect of fiber constraint due to the AFM indentation is less significant that the change in elastic modulus of the interphase region due to the interaction between fiber and matrix during curing process. Hence, this work confirms the distinct behavior of the near-fiber region in comparison to the surrounding matrix.

CHAPTER 5

VISCOELASTIC PROPERTIES

5.1 Introduction

Polymer materials are known to exhibit significant time-dependent behavior termed as viscoelastic behavior. This topic involves a good portion of research done on polymers that has been continued from the last two decades [68]. The large extent of time and temperature dependence of the mechanical properties of polymers, in comparison to metals, provides higher significance to the study of viscoelastic behavior of polymers. Interestingly, it has found many industrial applications. In short, polymers have some characteristics of an elastic solid and some of a viscous fluid. The molecular structure of polymers composed of long chains are highly linked to this behavior [69]. When a nano-scale outlook is considered, the flexibility of these polymer chains are known to be affected by its interactions with the surrounding system, which may be in the form of a reinforcement or an inclusion [70, 71]. This translates to modified mechanical and thermal properties of the polymer [72]. Hence, it is important to analyze the viscoelastic response of the distinct interphase region formed around the fiber in FRPs. Li and Weng [73] investigated the macro-scale effect of the viscoelastic interphase on the creep behavior of the fiber reinforced polymer composites. They concluded that the viscoelastic behavior of the interphase region has a strong influence on the creep strength and load-carrying capacity of the overall composite structure. Fisher and Brinson [72] showed the existence of an interphase region with viscoelastic moduli different from the bulk material using a theoretical approach based on Mori-Tanaka solution. Recently, Liu *et al.* [74] indicated in a review that AFM based indentations can be utilized to show the changes in viscoelastic behavior of the interphase region.

In this context, it is good to review the major aspects with regard to the evaluation of the viscoelastic properties using indentation technique, a powerful tool to determine properties at small length scales. In most of the cases, a simple load or displacement profile consists of a loading and an unloading region used to study the mechanical properties of the material - forming a triangular shape as shown in the fig 5.1a. This triangular profile is sufficient to characterize the elasto–plastic materials such as metals and ceramics where negligible time-dependent behavior may exist, as the load–displacement curve is quite insensitive to the rates of loading or unloading. However, the viscous nature of polymers creates time dependency in the unloading curve during indentation and this typically results in a "nose" region. This can be attributed to the excessive creep undergone by the material beneath the indenter and it overshadows the elastic recovery seen in materials as the tip moves up. It can considerably affect the estimation of elastic moduli using indentation technique [75]. A major fallback of this issue is that it gives a negative contact stiffness value or theoretically invalid fitting parameters, which doesn't allow the true evaluation of elastic properties of the material [76, 77]. From literature, it has been seen that the use of a dwell region (hold time) between the loading and unloading portion can be used to ensure that the material is completely relaxed so that viscoelastic recovery doesn't influence the unloading. This was shown by some of the recent indentation experiments done using a Berkovich indenter to indent into epoxy at varies dwell periods [78, 79].

The idea of using hold time in nanoindentation experiments was first introduced by Hochstetter *et al.* [80]. Since then there has been lot of interest to estimate the viscoelastic properties of polymers using this method [81, 82]. It is good to note that these indentation experiments can be conducted based on load control or displacement control mode. Accordingly, the viscoelastic response will generate creep curves or relaxation curves. As noted by Huang and Lu [83], for the analysis of stress and deformation, evaluation of relaxation modulus is essential. The relaxation modulus and creep compliance are related by Eq. (5.1).

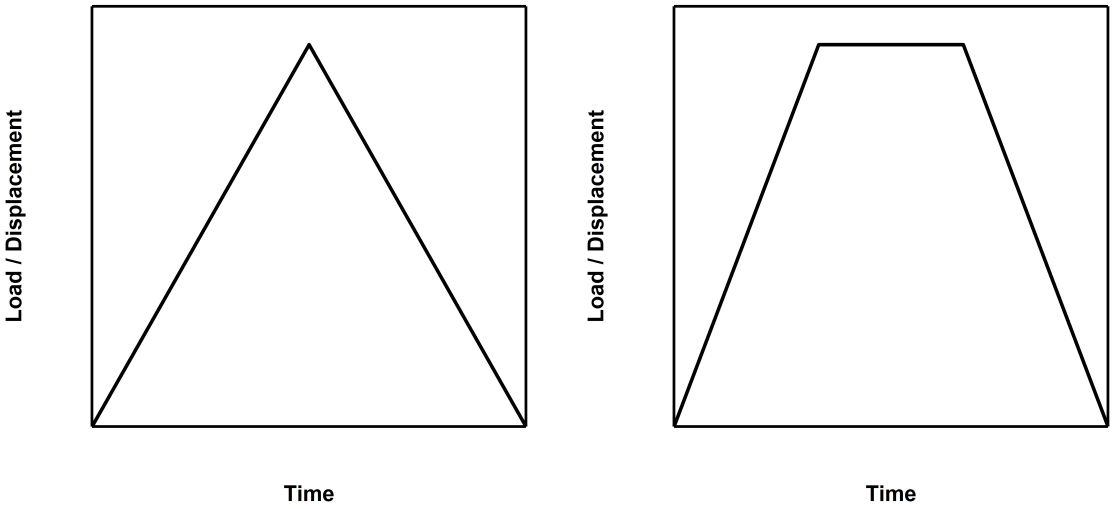

(a) Triangular (b) Trapezoidal

Figure 5.1: Indentation load or displacement profiles.

$$\int_0^t E(\xi)J(t-\xi)d\xi = 2(1+\nu)t \tag{5.1}$$

where, $E(t)$, $J(t)$ and ν are relaxation function, creep function and the Poisson's ratio. However, this relation has many limitations and a small error in the creep compliance will result in large errors in the determination of relaxation modulus. Therefore, in this study displacement controlled indentation experiments will be used to directly compute the relaxation modulus values. Displacement data obtained for different hold time will be used to analyze the stress relaxation of the material as a function of other parameters of the material system. Researchers have developed mathematical models for determining the stress relaxation or creep compliance using instrumented indentation techniques involving spherical and Berkovich nanoindenters for determining the viscoelastic behavior of polymers [83–85]. Also, these models have been successfully applied to study the variation of creep or stress relaxation behavior of the polymer as a function of different environmental factors or weight fractions of coupling agents used in composites [79, 86]. In the context of this study, the model provided by Shimizu *et al.* [87] will be used to determine the relaxation function $E(t)$. An application of a fixed indentation depth h_0 i.e. $h(t') = h_0 H(t')$

($H(t')$ is the Heaviside step function) will provide the constitutive relation for $E(t)$ (given in Eq. (5.2)) in terms of the load relaxation $P(t)$ captured during the constant indentation depth test.

$$E(t) = \frac{2\gamma}{gk}\frac{(1-\nu^2)}{{h_0}^2}P(t) \tag{5.2}$$

where, γ is a geometric factor dependent on the total penetration depth and contact depth using the relation $h = \gamma h_c$. g is the indenter shape factor given by $g = \pi \cot^2 \beta$ with β being the inclined face angle. k is known as the frontal factor and is related to the tip geometry as $k = \tan\beta$. In the case of the AFM indenter used in this study, $\beta = 79.3^\circ$ i.e. the angle between the half-space and the conical generators of the equivalent cone of the AFM indenter.

5.2 Use of AFM spectroscopy to determine viscoelastic response of the interphase

The unique ability of AFM tips to probe properties in nanometer scale as a function of distance from the fiber will be utilized to understand how the viscoelastic behavior of the interphase varies from the bulk material. Samples for the AFM indentation was prepared and imaged in the same manner as described above. The major difference in the analysis stems from the use of hold time (dwell) or the constant-rate displacement approach during the AFM indentation. In the first approach, AFM indentation is done in the displacement control mode, where the sample is loaded to a particular depth that is higher than the measured surface roughness of the sample. Thereafter, the displacement is kept constant for a finite amount of dwell period to study the stress relaxation and then unloaded. Hold times varying from 5s to 10s are employed to study the viscoelastic behavior. Displacement controlled indentation is used in this study so that the experimentally determined stress relaxation curves can be easily compared to the values obtained from the intended FEA based simulations. A typical load–displacement curve for this experiment is given in fig 5.2.

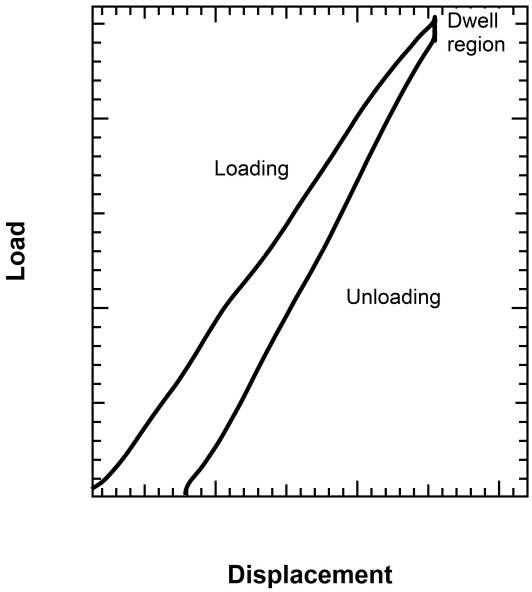

Figure 5.2: Typical load–displacement with a constant displacement based dwell region.

5.2.1 Relaxation curves of the interphase region

A constant displacement of 25 nm was used to study the near fiber region, based on the indentation depths observed from the previous experiments of this study. A small force of 100 nN was used to trigger the indentation and thereafter the indentation was carried out based on the input from the indenter panel. The general load profile for the experiments in this study is given in the fig 5.1b. As described in chapter 3, the adhesion map over a region approximately $1\mu m$ composing of the carbon fiber and near-fiber epoxy region was used to determine the contour of the fiber. MATLAB code discussed earlier was employed to generate radial lines from the fiber boundary to the matrix. The hold region data along these radial lines were subsequently analyzed to determine the relaxation curves. On an average there were 10,000 pairs of load–displacement data for a 5 sec hold time experiment and 20,000 pairs for a 10 sec hold time experiments. Due to the large volume of data, 4 radial lines were selected for the analysis and average of the viscoelastic response was computed. It is important to note that the data collected is masked by noise from internal sources of the equipment. Therefore, a low pass filter (LPF) was set-up using the corrected frequency

(determined during the calibration of the tip) at which the data was collected using the cantilever. This attenuates all the noise from the frequency higher than the cut off. An example of the filtered data is shown in fig. 5.3.

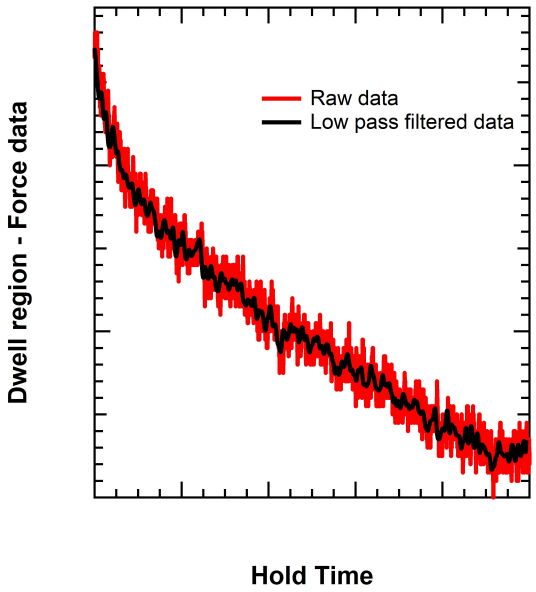

Figure 5.3: Low pass filtered data and the raw data collected from AFM.

The filtered load data was used in the model (Eq. (5.2)) to determine the relaxation modulus. The plot for normalized average relaxation modulus with respect to the hold time for 5 sec and 10 sec are given in fig. 5.4a and fig. 5.4b, respectively. These plots are an average of the data collected at different points along 4 radial lines to the carbon fiber boundary. The values are normalized for the purpose of understanding the variation in relaxation behavior of the epoxy as a function of the position of indent from the boundary of the carbon fiber.

The relaxation plots obtained from the AFM indentations are not smooth curves and include minor fluctuations which can be attributed to the small changes in the position of the AFM indenter as it is very small when compared to conventional nanoindentation tips like a Berkovich indenter. This is an inherent nature of the data collected using AFM tip. Therefore, the data has not been curve fitted. In both the plots, a significant amount of stress relaxation is observed at about 400 nm and 600 nm away from the fiber – that were

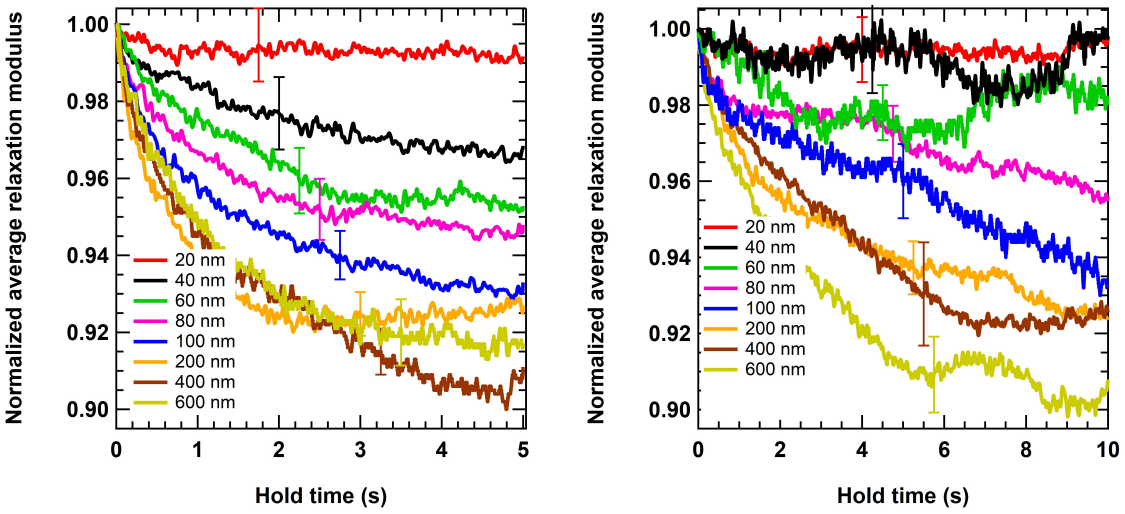

(a) 5 sec (b) 10 sec

Figure 5.4: Normalized average relaxation modulus as a function of the hold time.

previously identified as regions outside the interphase. As the hold time is increased, the stress relaxation tends to plateau which can be seen from the 10 sec relaxation plot. Taking into account the error bars involved, it is possible to state that there is very limited stress relaxation in the response of the interphase region when compared to the actual response of epoxy. Hence, it is demonstrated that the viscoelastic response of the interphase region is distinct when compared to the matrix. Additionally, it is good to note that the stress relaxation is significantly limited as the indents are done closer the fiber boundary. This is very important as it underscores the fact that viscoelastic response of the material around the fiber varies as a function of the distance from the carbon fiber. The sources for this behavior can be identified as the chemical interaction between carbon fiber and the epoxy or the fiber constraint effect.

5.3 Influence of fiber constraint on the viscoelastic response of interphase in CFRPs

5.3.1 Finite element modeling and material properties

The viscoelastic response of the interphase region can also be affected by the presence of the rigid fiber. Hence, a linear viscoelastic material model will be incorporated in the

material definition for FEA modeling of the AFM experiment to ascertain the impact of the rigid constraint on the determination of viscoelastic properties in the interphase region. The constant displacement data obtained from the hold time are fitted using Prony series given by the relation in the Eq. (5.3), based on the generalized Maxwell model. Thereby, the relaxation coefficients and relaxation times are obtained for the material definition to be used in the FEA simulation. These coefficients are added in terms of ratios of the instantaneous value.

$$E(t) = E_\infty + \sum_{i=1}^{N} E_i e^{-\lambda_i t} \tag{5.3}$$

where, E_∞ is the instantaneous value, E_i are the relaxation coefficients and λ_i are the reciprocals of relaxation times.

Additionally, a nonlinear elastic material definition is considered for the loading region as the FEA software doesn't take in plastic definition along with the viscoelastic properties. For this, the experimental data from the compression test was fitted to a reduced polynomial form of nonlinear elastic material model (given in Eq. (5.4) with N=1 i.e. Neo–Hookean form) using the FEA software and the corresponding material constants were empirically determined.

$$U = C_{i0}(\bar{I}_1 - 3) + \frac{1}{D_i}(J_{el} - 1)^{2i} \tag{5.4}$$

where, U, $\bar{I}_1$ and J_{el} are the potential, first strain invariant and elastic volume strain respectively. C_{10} and D_1 are the coefficients computed by the FEA software by fitting nominal stress and strain values from the compression test on epoxy.

Simulations are done similar to the method described in chapters 3 and 4 for the elasto-plastic material model, but in this case the step was modified as 'visco' to take into account the viscoelastic behavior of the material.

Table 5.1: Prony series constants obtained from curve fitting.

E_∞	E_1	λ_1	E_2	λ_2
2.48	0.265	0.843	0.109	4.987

5.3.2 Results of the constant displacement based simulations

Eq. (5.3) was used to fit the relaxation modulus curve for the material at 600 nm away from the fiber – this was taken as the response of epoxy. Two elements of the generalized Maxwell model was used and the Prony series constants i.e. relaxation coefficients and relaxation times determined are given in table 5.1.

The simulations were done for 5 sec hold time by placing the point of indent at varying distance from the rigid constraint. Fig. 5.5 shows the variation of the normalized relaxation modulus for the different indents performed and compares it to the previously obtained experimental data.

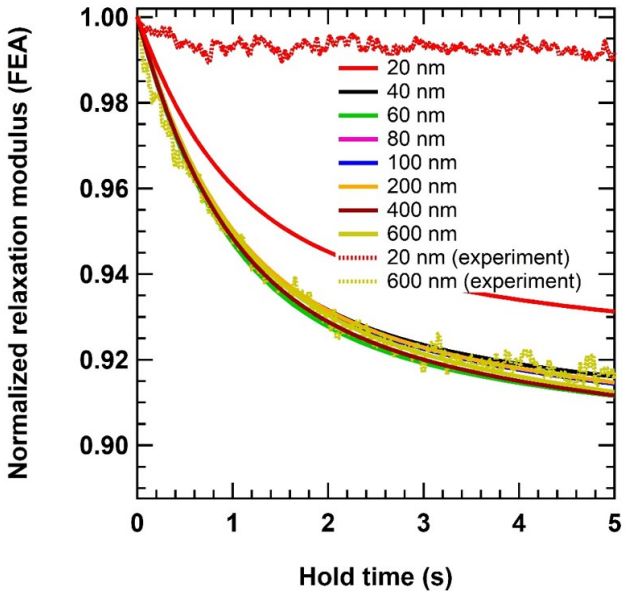

Figure 5.5: Comparison of normalized relaxation modulus evaluated from experiment and 3D FEA data.

It can be observed from fig. 5.5 that the viscoleastic response of epoxy from FEA is comparable to the experimentally determined values. Therefore, the results obtained from

the simulation model can be compared to experimental results to ascertain the extend of influence of fiber constraint effect. The major point to note in fig. 5.5 is that only for the 20 nm indent, there is a significant deviation in the viscoelastic response obtained. This infers that only for indents within the region of 20 nm away from the carbon fiber, the constraint contributes approximately 3% reduction in the stress relaxation. However, it can seen that the experimentally determined stress relaxation modulus for material at 20 nm away from the fiber is approximately 10% less than the response of epoxy. Hence, it can be conclusively stated that the viscoelastic behavior of interphase region is different from the bulk material due to its interaction with carbon fiber.

5.4 Conclusion

Polymer materials are known to exhibit time dependent behavior. For the first time, an AFM indentation based approach was proposed to determine the changes in viscoelastic response of the interphase region along a radial line and compare it to the response of the bulk material. This approach involved constant depth based AFM indentation, in which the stress relaxation during varying hold times (1 sec to 10 sec) were analyzed. Results showed that along a radial line to the carbon fiber, there is a decreasing rate of stress relaxation in the material. Quantitatively, it was observed that the stress relaxation of the material at 20 nm away from the fiber was about 10 % less than that for the material at 600 nm away from the fiber. It denotes that the viscoelastic response of the interphase is distinct from the bulk material. For the first time, the effect of fiber constraint on the viscoelastic response observed using indentation technique was also computed.

Prony series based curve fitting was done to the relaxation modulus curve obtained at 600 nm away from the fiber. The relaxation coefficients and the reciprocals of the relaxation time for a two element system were evaluated by Prony series curve fitting. It was used as the material definition for the linear viscoelastic behavior in conjunction with a nonlinear elastic behavior defined for the loading region. FEA simulations based on constant dis-

placement indicated that only for indent at 20 nm away from the fiber, there is a marginally small effect of fiber constraint on the stress relaxation. Hence, it can be concluded using the numerical approach that the viscoelastic response of the material is affected by its proximity to the carbon fiber and the chemical interaction between the fiber and the matrix.

CHAPTER 6

EFFECT OF UV IRRADIATION ON INTERPHASE PROPERTIES

6.1 Introduction

As an example application, the AFM indentation technique was applied to investigate the impact of UV irradiation on the mechanical properties of the near-fiber region. Exposure of polymers to UV leads to the absorption of photons and the activation of polymer macromolecules that cause the formation of free radicals and breaking of bonds, which over extended periods of exposure will lead to the failure of the polymer [88]. Chemical structure of the polymer is changed primarily by chain scission which leads to the formation of functional groups with double bonds such as C=C and C=O. These functional groups involve in the photocatalytic degradation process leading to the discoloration and degradation of the polymer. Additionally, these new reaction sites contributes to crosslinking [88].

Mailhot *et al.* [2] examined the possible chemical changes that occur in epoxy due to exposure to UV. They investigated the photooxidation mechanism of diglycidyl ether of bisphenol-A (DGEBA) and amine based hardner. It was noted that there can be occurrence of three major chain scissions. Two of which is involved with the oxidation of the isopropylidene site shown in fig. 6.1. It results in the photo–products such as acetophenone and benzyl methyl ketone. In the case of formation of acetophenone, β–scission can produce it as an end group (scission 'a') or as an in-chain group (scission 'c'). The third possible scission reaction involves the disappearance of ether group (CH_2) as shown in Fig. 6.2 and the breaking of the $CH_3 - C$ bond.

Overall, it can be understood that variations in the properties of these polymers are dependent on the amount of chain scission and also the possible subsequent crosslinking

(formation of new covalent bonds between the chains or recombination of radicals) that can occur during its exposure to UV. This is corroborated by Woo *et al.* [88], where brittle fracture of epoxy due to UV embrittlement with limited amount of plastic deformation was observed. It was also noted that the rate of degradation is very rapid initially and shows slight increase with further exposure to UV irradiation.

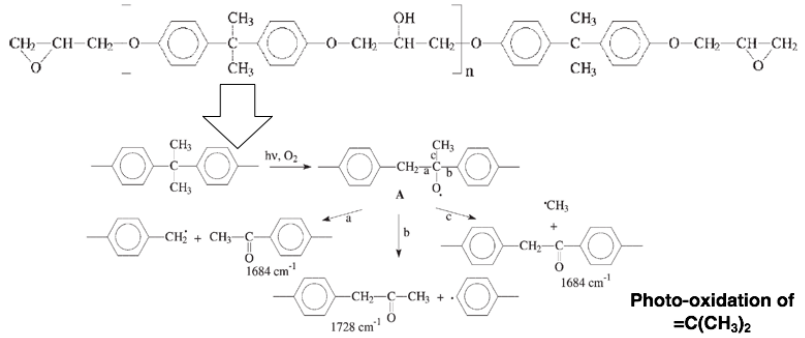

Figure 6.1: Photo–oxidation of $=C(CH_3)_2$. (Adapted from Mailhot *et al.* [2])

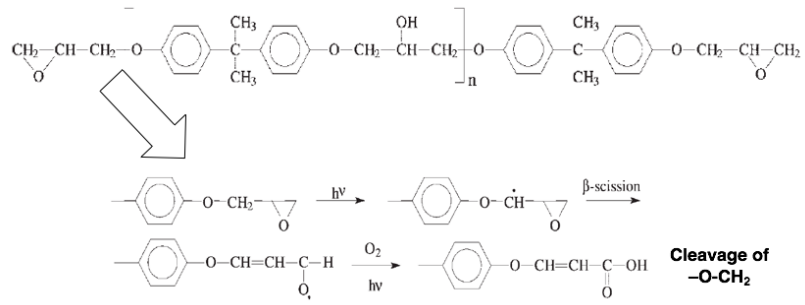

Figure 6.2: Cleavage of $-O-CH_2$. (Adapted from Mailhot *et al.* [2])

The photo-degradation of carbon fiber by UV irradiation is also an important aspect that influence the overall effects of UV exposure on the polymer matrix composite. This is beacuse the photo-degradation of carbon fiber can produce free radicals that then affect the polymer, especially in the interphase and near–fiber region. Mulyana *et al.* [89] investigated the effect of UV irradiation on graphene, which is very closely matched in terms of chemical bond structure with the carbon fiber. It was revealed that exposure to UV results in the photocatalytic degradation of the material. In this process, the $C-C$ bonds are broken and subsequently multiple linkages with oxygen are formed. However, these bonds break

giving rise to generation of $\dot{O}$ free radicals. A similar degradation process may be followed by carbon fiber under UV irradiation. Therefore, it is very important to consider how UV irradiation impacts the overall behavior of carbon fiber reinforced epoxy composite.

Awaja *et al.* [60] indicated that the type of reinforcement influences the response of matrix such as epoxy due to the degradation by UV exposure. They observed that carbon fiber reinforced epoxy underwent chain scission and cross-linking reactions during UV irradiation. X-ray photoelectron spectroscopy (XPS) of UV exposed CFRP revealed an increase of 108% in carbonyl species (C=O), which indicated the impact of surface oxidation. It was noted that the increase in reaction sites resulting from chain scission leads to more opportunities for oxygen and nitrogen to form bonds with polymer, thereby causing a rise in cross-linking reactions. It is important to note that the possibility of matrix degradation being affected by photo-catalysis of the reinforcement was examined by Awaja *et al.* [60] based only on the chemistry. There is lack of clarity regarding the measure of influence of photo-degradation of carbon fiber on the matrix in terms of the mechanical properties and the proximity to the reinforcement. The three key factors for this investigation include distinct properties of the interphase, variation in response closer to the fiber and time-dependent behavior of the polymeric material considered. Hence, this study will examine the influence of UV irradiation on the interphase region and bulk material as a function of the time exposed to UV and distance from the boundary of the fiber. AFM indentation based force spectroscopy will be utilized to capture the variations in response along a radial line from the fiber.

6.2 Methodology

For this study, the cross-section surface of carbon fiber–epoxy specimen was exposed to ultraviolet radiation (UV) at 0.7 W/m^2 at 70°C for time periods varying from 30 minutes to 24 hours using QUV accelerated weathering tester (Q-labs, Westlake, OH, USA). This intensity replicates quite closely the average UV irradiation of sunlight, which is in the

range of 0.65 to 0.7 W/m^2. Thereafter, AFM based force spectroscopy was used to study the properties of these samples. For understanding the variation in modulus radially from the carbon fiber, a MATLAB code was employed, as explained in Chapter 3.

Data from two regions of the CFRP samples were collected. The first one is the response of the bulk material, taken from indentations across a region of 5μm performed at approximately 8 mm away from the fiber. Second is the interphase properties obtained by performing force spectroscopy in the near–fiber region of about 1μm.

To study the viscoelastic response, a dwell time of 5 sec was applied at constant load of 1.78 μN was incorporated in the force spectroscopy. Similar to the procedure indicated in chapter 3, the adhesion map was used to distinguish the boundary of the fiber and evaluate the distance of the indent from the periphery of the fiber. The displacement data was filtered using a low pass filter designed similar to the approach given in chapter 4. A creep compliance model that was developed by Tweedie *et al.* [84], given in Eq. (6.1) was used to compute the creep behavior at the different points from the boundary of the fiber.

$$J_c(t) = \frac{8 * \tan\alpha * h(t)^2}{\pi * P_0} \tag{6.1}$$

where, α is the semi-apex angle of the AFM indenter, which has a value of 70.3 °. P_0 is the constant load applied and $h(t)$ is the displacement data collected from the constant load dwell period.

Additionally, an ATR–FTIR spectrometer (Agilent Cary 680, Agilent Technologies, Santa Clara, California, USA) was used to perform absorbance mode spectroscopy on the surface of epoxy–bulk material exposed to different time periods of UV radiation. The spectra for each type were collected from two samples each between the wavenumbers varying from 4000 cm^{-1} to 400 cm^{-1} using 64 scans. A characteristic IR chart was used to interpret the spectra of each sample.

6.3 Results and discussion

6.3.1 Variation in elastic modulus of bulk material as a function of UV exposure

The elastic modulus maps of the cross-sectional surface of carbon fiber reinforced epoxy under pristine condition and subjected to UV irradiation ranging from 30 minutes to 24 hours were obtained by AFM force spectroscopy. Select modulus maps are shown in the Fig. 6.3. Modulus maps for each sample were created using a 48×48 square grid, which implies there are 2304 load–displacement curves. It can be visually ascertained from the modulus maps that the elastic modulus of epoxy away from the fiber has decreased as a function of prolonged exposure to UV radiation. This is consistent with the formation of free radicals as epoxy undergoes chain scissions due to UV irradiation, making it comparatively less stiff, as discussed earlier. The elastic modulus of pristine epoxy decreased almost linearly from 2.8 ± 0.23 GPa to 1.9 ± 0.26 GPa after 24 hours of UV irradiation as shown in Fig. 6.4. This indicates that there is a drop of 32% in the elastic modulus for epoxy when subject to UV for 24 hours. The reported modulus values are the average from all the indents shown in the modulus map.

The changes in the elastic modulus of epoxy due to UV irradiation follows a similar decreasing pattern as described by some of the past work that studied influence of UV on neat epoxy and addition of fillers for the same time period considered in this study [88, 90]. Woo *et al.* [88] performed tensile experiments on neat epoxy samples subject to UV irradiation. They found a decrease in tensile modulus of about 6% after about 250 h of UV exposure. It is significantly lower than the variation captured in this study. This can be attributed to the influence of UV irradiation taken as a surface measurement on the CFRP samples compared to other studies that have evaluated impact on the overall behavior.

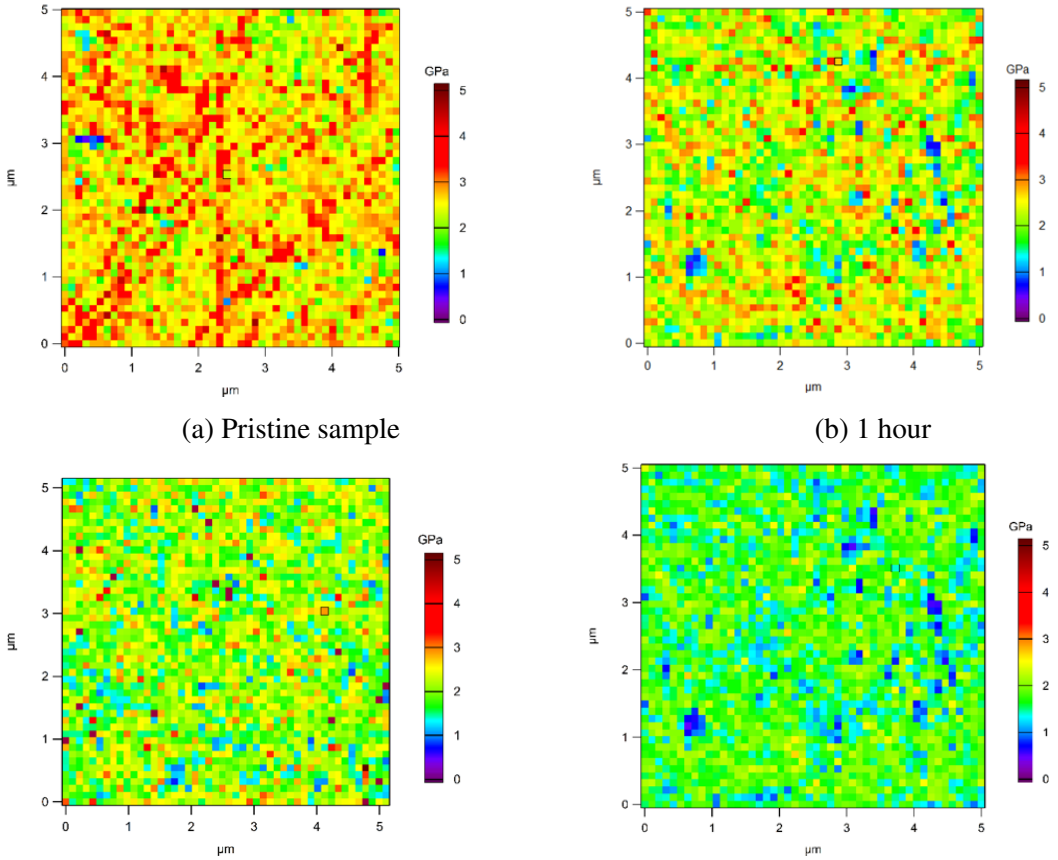

(a) Pristine sample

(b) 1 hour

(c) 6 hours

(d) 24 hours

Figure 6.3: Modulus map of epoxy region exposed to UV for different time periods (5μm, Scale: 0 to 5 GPa).

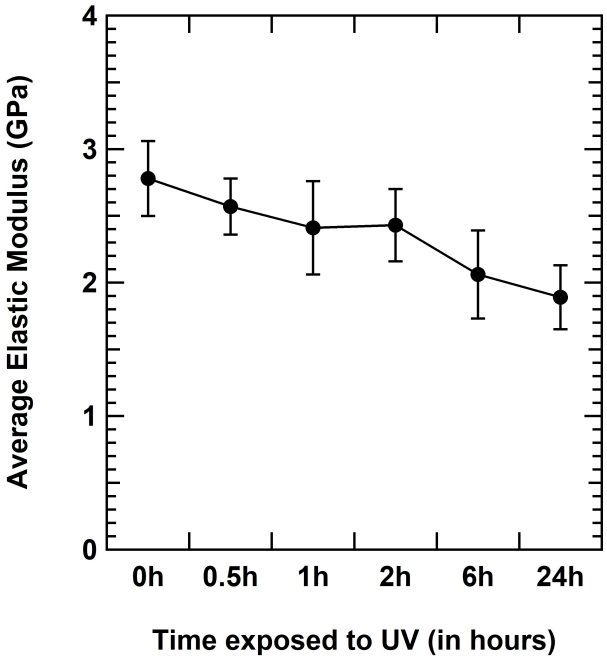

Figure 6.4: Variation in elastic modulus of neat epoxy as a function of time exposed to UV.

6.3.2 Viscoelastic behavior of the bulk material subject to UV irradiation

It is expected that the time dependent response of epoxy will also be impacted by the UV irradiation. Here, the variations in creep behavior of epoxy approximately at 8 mm away from the fiber is monitored as a function of time exposed to UV irradiation, as shown in fig. 6.5. After 2 hours of exposure to UV radiation, the creep compliance at the end of 5 sec increased by approximately 40%. This certainly points to the fact that chain scission reactions occur in the epoxy due to the exposure to UV, as discussed in the previous section. However, unlike the elastic modulus which deteriorates further with exposure to UV the creep behavior shows a reversal. Creep compliance curves evaluated after 6 hours and 24 hours of UV irradiation shows that the material has become considerably creep resistant compared to the pristine condition. A force spectroscopy done on the 24 hours UV exposed sample without the dwell time showed that elastic modulus was approximately 1.8 GPa, which is consistent with previously obtained data.

This reason why such a reversal occurs can be due to oxidation of the surface due to

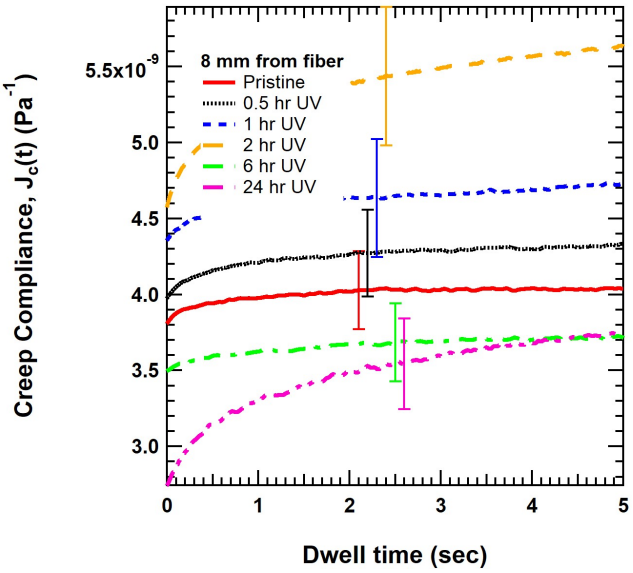

Figure 6.5: Variation in the creep compliance, $J_c(t)$, of epoxy at 8mm away from the fiber as a function of time exposed to UV radiation.

exposure to the UV also occurs simultaneously. This surface phenomenon is verified with the help of Fourier Transform Infrared (FTIR) spectroscopy of samples exposed to 1 h and 24 h of UV irradiation. Fig. 6.6 shows the FTIR spectra of the exposed epoxy surface. The peaks between 1900 cm^{-1} to 1200 cm^{-1} are only shown to focus on the changes between the two spectra.

It can be clearly observed from the fig. 6.6 that extended exposure to UV irradiation has developed two distinguishable peaks at A – 1675 cm^{-1} and B – 1725 cm^{-1}. This corresponds to formation of aldehydes and ketones with $C = O$. From literature, it is supported by the peaks corresponding to acetophenone (1685 cm^{-1}) and benzyl methyl ketone (1725 cm^{-1}) [2]. It is possible to consider that the continued generation of these functional groups could contribute to the reversal in the creep behavior upon exposure to UV irradiation. The other possible reason can be that the material was subject to temperature near its glass transition temperature for a considerable amount time. Since the reversal in response is not seen in the case of elastic modulus, it can be speculated that the time dependent properties shows the effect of subsequent crosslinking earlier than the glassy behavior. The possibility

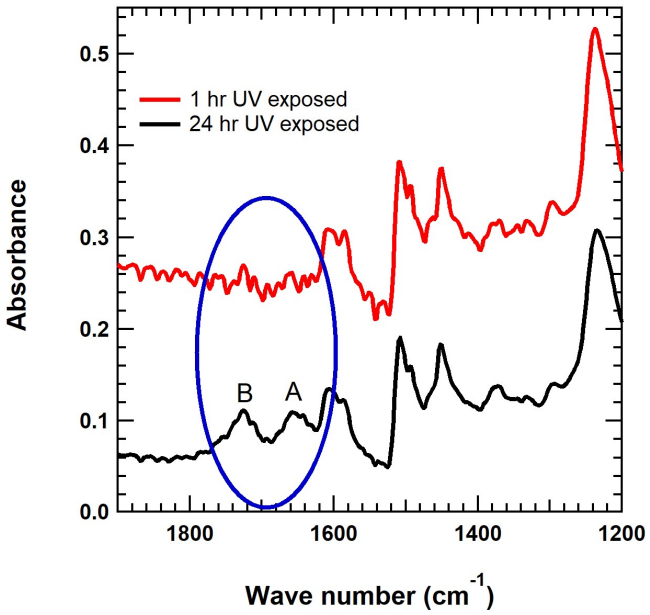

Figure 6.6: FTIR spectra of epoxy surface exposed to different time periods of UV irradiation (A – acetophenone and B – benzyl methyl ketone).

of smaller chains can also lead to less mobility. Also, exposure to UV irradiation for longer duration may help to capture the reversal in response in terms of elastic modulus as well.

In this context of studying the behavior of epoxy as a function of different time periods of UV exposure, it is important to examine the effect of proximity to the reinforcement on the material response. The next section discusses the impact of UV irradiation on mechanical properties of epoxy as a function of both distance from the carbon fiber and time period of exposure.

6.3.3 Changes in elastic modulus of near–fiber region due to UV irradiation

To study the impact of UV irradiation in near fiber region, elastic modulus maps across 950 nm square region containing the fiber and the interphase were obtained for pristine condition and those subjected to time period of UV irradiation ranging from 30 minutes to 24 hours of UV irradiation. Select modulus maps obtained are given in fig. 6.7. It can be observed that is severe distortion in fiber contour as well as significant changes in the properties of the near fiber region due to UV irradiation.

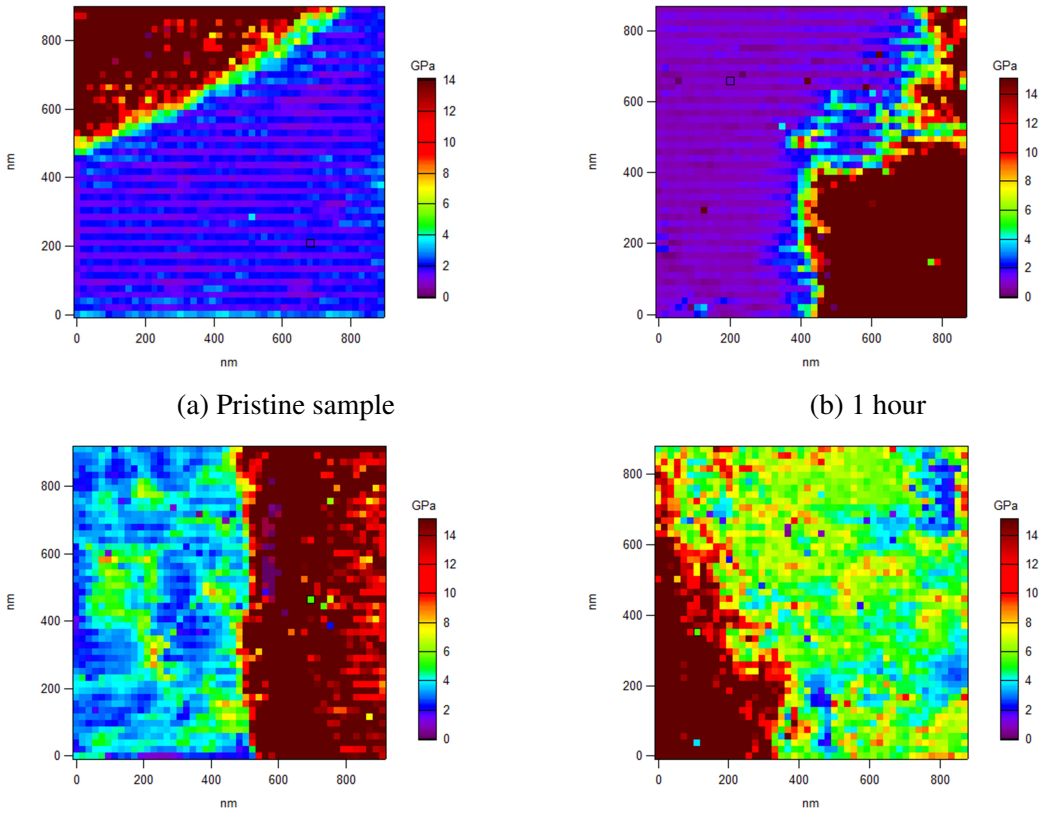

(a) Pristine sample

(b) 1 hour

(c) 2 hours

(d) 6 hours

Figure 6.7: Modulus map of fiber–matrix interphase region exposed to UV for different time periods (950 nm, Scale: 0 to 15 GPa).

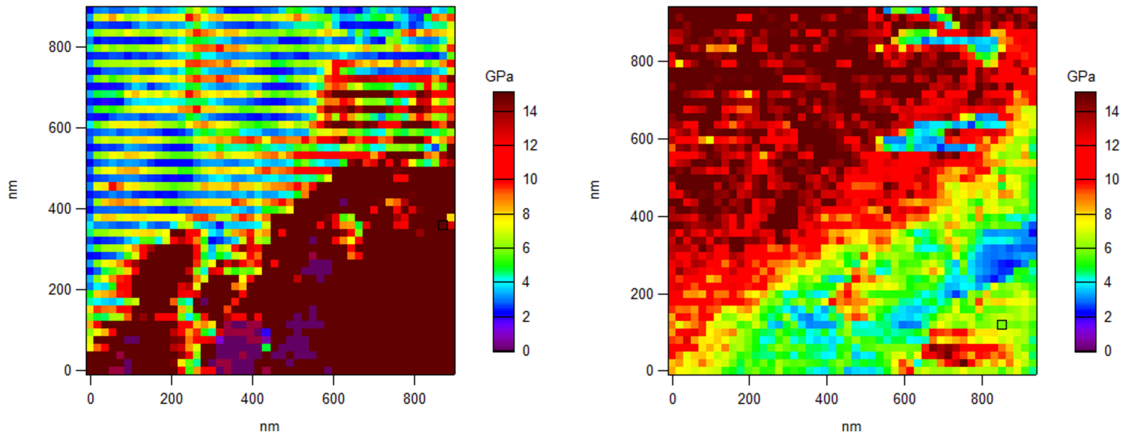

Figure 6.8: Modulus maps of near–fiber region of different carbon fibers in the 6h UV irradiated sample.

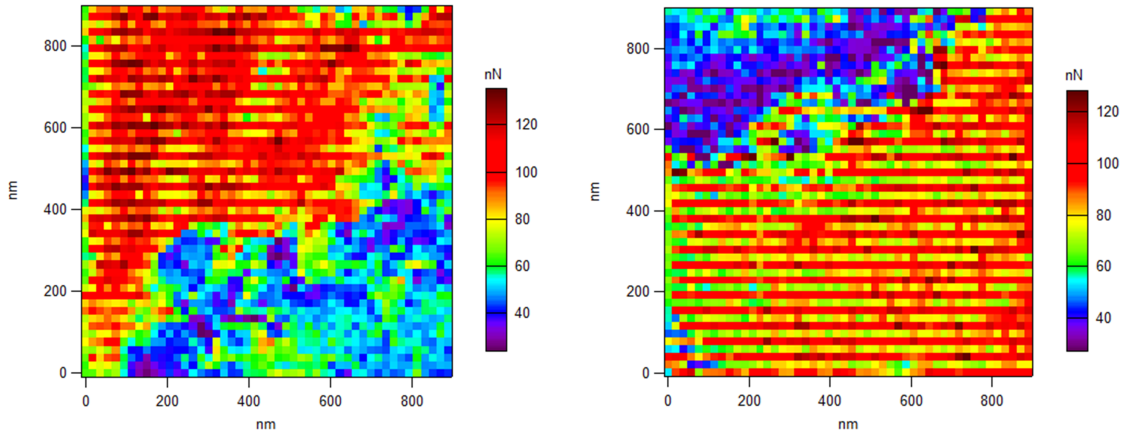

Figure 6.9: Adhesion maps of near–fiber region of different carbon fibers in the 6h UV irradiated sample.

Figures 6.8 and 6.9 shows the modulus maps and adhesion maps of force spectroscopy done on different carbon fibers in the sample that was exposed to 6 hours of UV irradiation. It can be clearly seen that the boundary of the carbon fiber is distorted upon 6 hours of exposure to UV radiation. This can be attributed to the photocatalytic degradation of the carbon fiber, which was discussed previously.

The MATLAB code that was previously described was employed to analyze the modulus values of CFRP along radial lines from the fiber. Fig. 6.10 compares the average modulus values at different radial distances from the fiber in CFRP to the modulus value of epoxy significantly far away from the vicinity of the fiber, as a function of time exposed to UV radiation. Due to the difficulty to ascertain the contour of the carbon fiber because of severe distortion of the carbon fiber, the modulus map of interphase region after 24 hours of UV irradiation was not included in the data analysis using the MATLAB code. It can be noted from Fig. 6.10 that the modulus values at 20 nm and 40 nm away from the fiber decreases rapidly when it is initially exposed to UV radiation, compared to the decrease in modulus values at 100 nm and 600 nm. This can be attributed to the significant amount of chain scission that occurs around the fiber due to the photocatalytic degradation of carbon fiber. This causes the breaking of C–C bonds that leads to formation of $\dot{O}$ free radicals and

new reaction sites near the fiber. After 1 hr of UV irradiation, it can be observed that the modulus values at 20 nm, 40 nm, 100 nm and 600 nm rises due to the increase in cross-linking reactions. Hence, after 6 hours of UV irradiation the modulus value of epoxy at 600 nm away from the fiber was about 162% higher than the modulus value of epoxy evaluated approximately 8 mm away from the fiber. The modulus of epoxy at about 8 mm away from the fiber decreased monotonically as a function of time exposed to UV radiation due to photo-degradation of epoxy and its response was not influenced by the presence of carbon fiber. Nonetheless, it can be observed that after 6 hours of UV irradiation epoxy at 20 nm and 40 nm away from the fiber, showed an overall decrease of 44% and 30%, respectively. It can be attributed to the weakening caused by photocatalytic degradation of the carbon fiber. Whereas, the modulus value of epoxy at 100 nm and 600 nm after 6 hours of UV irradiation indicated an increase of 68 % and 124 %, respectively. This clearly demonstrates that the presence of carbon fiber as reinforcement significantly influences the response of epoxy to UV irradiation.

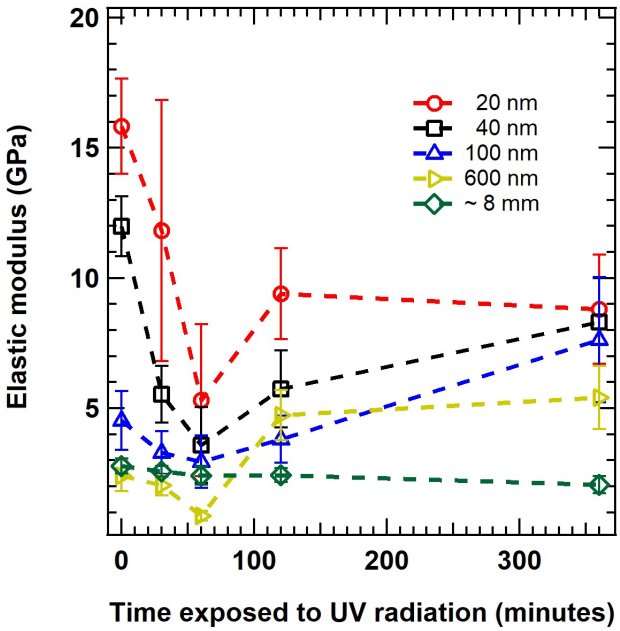

Figure 6.10: Variation in the elastic modulus, E, of CFRP as a function of position of indent from the fiber for different time periods of UV exposure compared to epoxy sample.

In this regard, AFM based force spectroscopy is also employed to study the effect of

UV irradiation on the viscoelastic response of the near-fiber region.

6.3.4 Influence of UV irradiation on the viscoelastic response of the near–fiber region

The creep compliance of the sample in pristine condition was evaluated initially for a reference to study the impact of UV irradiation, as shown in fig. 6.11. It can be very clearly observed that there is a significant change in the viscoelastic response of the material to a constant load based on the position of the indent from the carbon fiber. The behavior of the material closer to the fiber is more creep resistant compared to the response further away from the fiber. This is quite consistent with the constant displacement data discussed in chapter 5 as a function of radial distance to the fiber. It can be seen that there is very less relaxation of the load near the fiber compared to the results obtained at 600 nm from the fiber. This behavior by the near fiber region can be attributed to the interaction of the polymer with the carbon fiber and the formation of the distinct layer of the interphase. As discussed earlier, polymers such as epoxy generally exhibit significant time dependent behavior. Hence, as expected the response of the material further away from the fiber is considerably more creep compliant, taking the error bars into confidence.

Figure 6.12 shows the viscoelastic response of the sample exposed to 6 hours of UV irradiation as a function of the distance to the fiber. There are few takeaways from the comparison of the two figures. One, the viscoelastic response of the material is still dependent on the position of the indent with respect to the fiber. In other words, after 6 hours of UV irradiation the viscoelastic behavior is distinct taking into consideration the error bars of the creep compliance curves. This denotes that degradation of the carbon fiber as well as the proximity of the material to the fiber are factors influencing the behavior of the material. Additionally, it can be noted that at 20 nm from the fiber, at the end of 5 sec dwell period the material has become creep compliant by approximately 30%. Whereas, at 600 nm from the fiber the material showed enhanced creep compliance of only 3% at the end of the dwell time. This indicates that degradation of the carbon fiber discussed previously

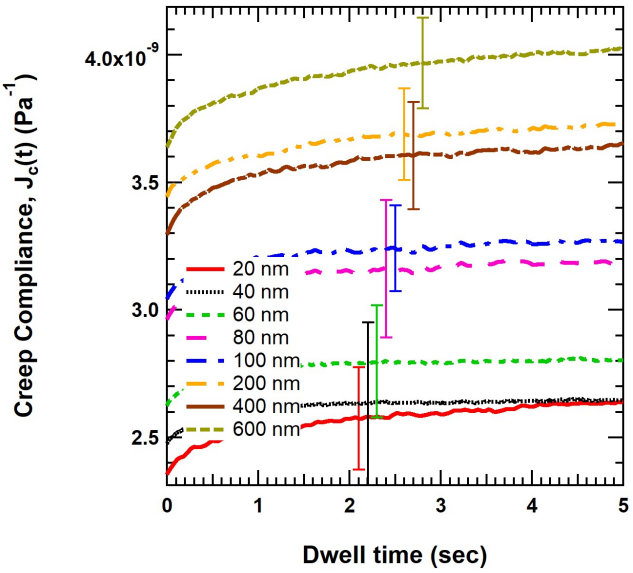

Figure 6.11: Variation in the creep compliance, $J_c(t)$, of CFRP as a function of position of indent from the fiber under pristine condition.

in this chapter has led to significant breaking of bonds in the interphase region.

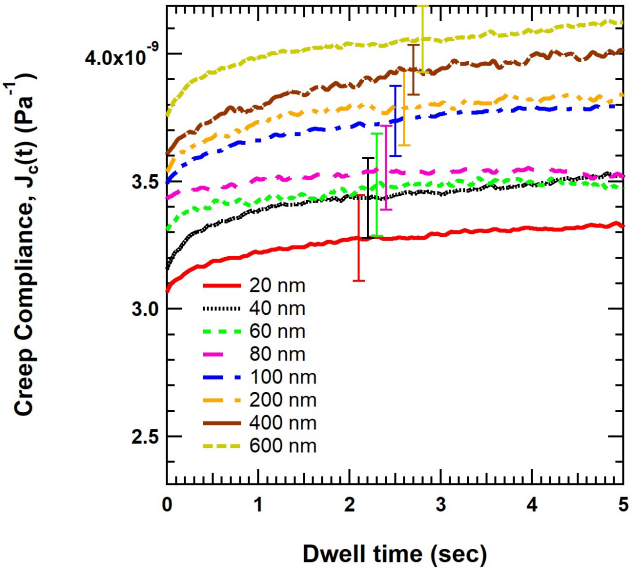

Figure 6.12: Variation in the creep compliance, $J_c(t)$, of CFRP as a function of position of indent from the fiber after 6 hours of UV irradiation.

In this context, it is essential to examine the influence of the duration of exposure to UV irradiation at different radial distance from the fiber. Fig. 6.13 shows the changes in creep behavior as a function of time exposed to UV irradiation at 20 nm, 40 nm, 100 nm and 600

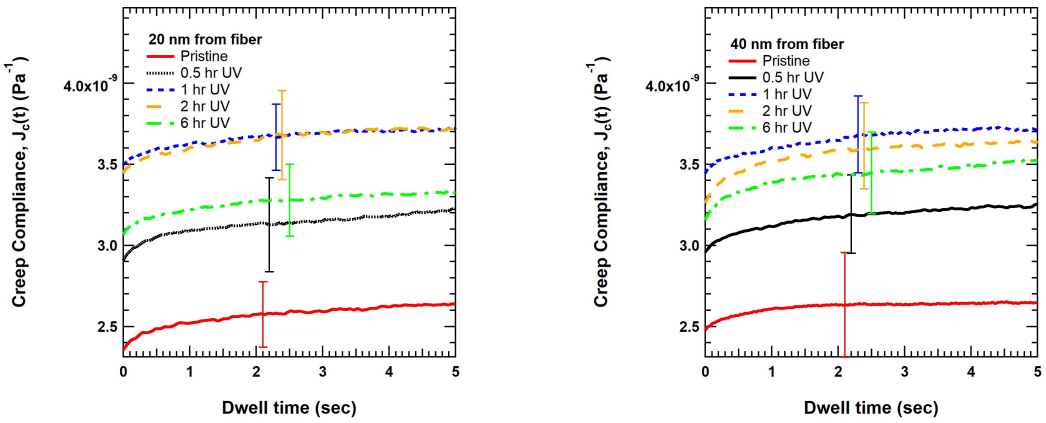

(a) 20 nm

(b) 40 nm

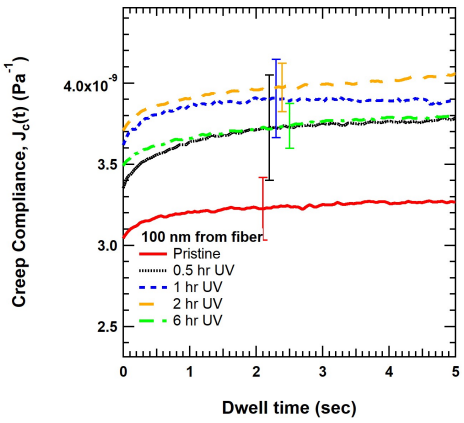

(c) 100 nm

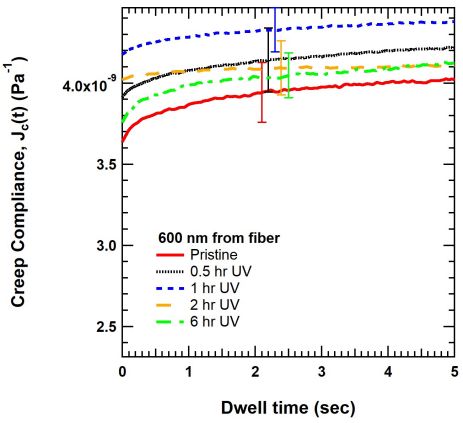

(d) 600 nm

Figure 6.13: Change in creep behavior as a function of time exposed to UV irradiation at different radial distance from the carbon fiber.

nm away from the fiber.

Fig. 6.13a and 6.13b indicates that at 20 nm and 40 nm the material becomes creep compliant by approximately 25% after 30 minutes of exposure to UV radiation. This can be attributed to the chain scission reaction of epoxy, which was described previously and also due to the deterioration of the carbon fiber. However, it can be observed that after 2 hours of UV exposure the material tends to be comparatively creep resistant. This trend is similar to the variation observed in the elastic modulus. The creation of new reaction sites by the initial incidence of UV radiation leads to further cross-linking, which can be the reason for the reversal of behavior. This can be seen in the case of the changes in response of the region at 100 nm from the fiber, as shown in the fig. 6.13c. However, the material

tends to be creep resistant at the observation for 6 hr of UV irradiation instead of the 2 hr UV irradiation seen in the case of 20 nm and 40 nm. These three distances lie within the identified interphase region and hence it can be ascertained that the proximity to the carbon fiber affects the viscoelastic response of the material subject to UV radiation along with the time corresponding to the change in creep behavior.

In the case of 600 nm away from the fiber, shown in fig. 6.13d the creep compliance curve for pristine condition matches very closely with response obtained about 8 mm from the fiber. However, it can be noted that there is a significant drop in the increase of creep behavior of the material due to exposure to UV compared to other indents done closer to the fiber. Although the material undergoes chain scission reactions, from 2 hours of UV exposure the material shows relatively creep resistant behavior possibly due to the oxidation of the epoxy region. This is consistent with the trend seen in the case of indents done at about 8 mm from the fiber, barring the time period when the reversal of behavior initiated. This difference may be closely related to the influence of proximity to the reinforcement.

6.4 Conclusion

The use of force mapping technique to evaluate properties very close to the fiber was extended to study the effect of environmental factors on the interphase behavior. It was used to evaluate the impact of UV irradiation on the elastic modulus value as a function of exposed time and radial distance to the carbon fiber. It was observed that the response of epoxy to UV irradiation is dictated by the proximity to the carbon fiber. An initial decrease in modulus of interphase region was observed due to the photocatalytic degradation of the carbon fiber. It leads to chain scission reactions that causes formation of free radicals and new reaction sites. However, it was noted that upon further exposure to UV irradiation the interphase modulus values increased on account of the enhanced cross–linking reactions. Hence, it can be indicated that the presence of carbon fiber hinders the photo-degradation of epoxy i.e. reinforcement of carbon fiber could improve the durability of the composite

structure.

The viscoelastic response of the material was also examined as a function of time exposed to UV irradiaiton. It was observed that the material initially becomes significantly creep compliant. But after continued exposure to UV radiation, the response becomes relatively creep resistant. Also, the variation in the creep compliance curves capture the influence of deterioration of the carbon fiber on the response of the surrounding region. Finally, the oxidation of bulk material possibly causes epoxy to be creep resistant upon continued exposure to UV irradiation.

CHAPTER 7

INFLUENCE OF THERMAL MISMATCH BETWEEN FIBER AND MATRIX

7.1 Introduction

The properties of the interphase region in composites are influenced by several processes involving chemical, mechanical and thermal interaction between the matrix and the fiber. This directly or indirectly contributes to the existence of an interphase that posses distinct properties compared to the bulk material. Previous chapters captured the overall variation in the interphase properties along with the impact of fiber constraint on the evaluation of the properties in the near–fiber region. In this chapter, the focus is on the mismatch in the coefficient of thermal expansion (CTE) of the matrix and the fiber, along with its impact on the determination of the interphase behavior. Past studies have pointed out that the cooling of the composite after post curing causes the presence of thermal residual stresses in the matrix, fiber and as well as the interphase region [91, 92]. These residual stresses may adversely or positively impact the overall behavior of the composite and the interfacial adhesion between the fiber and the matrix. It has been previously demonstrated by Penn *et al.* [93] that a smaller thermal mismatch causes reduced thermal stresses and a weaker interphase in the case of aramid–epoxy composite.

The generation of residual stresses in the interphase can be attributed to other factors such as shrinkage during curing, differences in the morphology of the matrix and non-uniform solidification of the matrix [63, 91]. Nonetheless, in this study the influence of thermal mismatch of the fiber and matrix are closely analyzed. In the case of carbon fiber reinforced epoxy, the carbon fiber and the epoxy have CTE that are very different. The carbon fiber has a negative CTE in most cases and epoxy shows a positive CTE [61]. This dif-

ference has an important effect on the properties of the interphase and its width. Some micromechanical models of fiber reinforced composites have indicated that the development of residual stress are due to the processing techniques employed [94–96]. Hardiman *et al.* [97] analyzed the impact of microscale thermal residual stresses on the properties of fiber reinforced composites. Modeling of nanoindentation technique is employed to capture the presence of the stresses from thermal cool down. Results indicate the sensitivity of the properties determined by nanoindentation technique to the existence of the residual stresses. However, there is still a lack of understanding on the impact of this contrasting behavior on the evaluation of the properties very close to the fiber at a nanoscale.

This study will utilize the AFM indentation based force spectroscopy to examine the variation of elastic modulus along a radial line for a carbon fiber reinforced epoxy sample that was not subject to post curing at 121°C. Additionally, finite element (FE) simulation of AFM indentation is carried out on a substrate heated to 121°C and thereafter cooled to room temperature. This approach is believed to provide good knowledge about the influence of thermal stresses on the interphase properties at very small length scales and its correspondence to the width of the interphase region.

7.2 Experimental analysis of effect of post curing

7.2.1 Material preparation

Circular samples of carbon fiber reinforced in epoxy were prepared by curing epoxy at room temperature for 24 hours, as required. Unlike the material preparation described in Chapter 3, the CFRP samples in the case were not subject to post curing at 121°C. As previously indicated, surface roughness is an important factor that affects the data collected during AFM indentation. Hence, thin circular strips of samples were cut and then subject to metallographic polishing techniques. The RMS value of the resultant surface of the sample was determined using AFM imaging to be 5.7 nm.

It is essential to examine the properties of the epoxy that is not subject to post curing

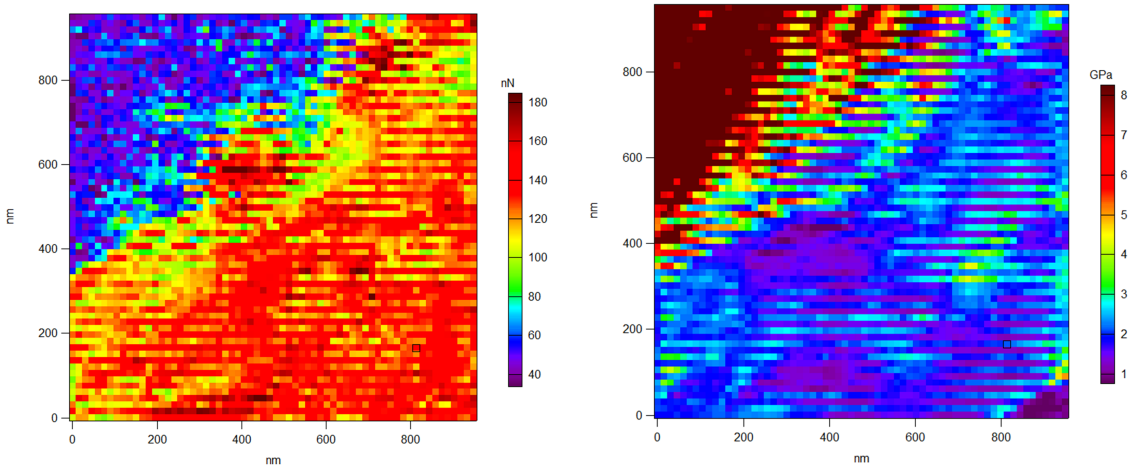

(a) Adhesion map (b) Modulus map

Figure 7.1: Force spectroscopy of the interphase region of 'not post–cured' CFRP sample.

as it can be used for the generation of the modulus map. Therefore, 3 epoxy samples of the said material preparation method were subject to compression tests as per ASTM standards [67]. The average elastic modulus value was determined to be 1.03 ± 0.82 GPa, which is significantly lower than a post cured epoxy sample.

7.2.2 Force spectroscopy of the near–fiber region

The methodology for AFM force spectroscopy used in chapter 3 was followed in this step along with the calibration of the AFM tip. A 64×64 grid was used over a square region of 980 nm to capture the behavior of the carbon fiber, the matrix and the interphase region. Fig. 7.1a indicates that the adhesion of the tip on the carbon fiber surface is significantly lower than the matrix region, which is epoxy in this case. This is utilized to distinguish the boundary of the carbon fiber and the epoxy in the modulus map given in fig. 7.1b. Furthermore, the data was analyzed with the aid of the MATLAB code given in the appendix.

The compression modulus value of epoxy previously obtained from the compression test was used as a reference to plot the modulus map. Fig. 7.2 shows the radial distribution of the modulus values as a comparison between the sample that was 'post–cured' and 'not post–cured'. The data points are an average of values obtained from 6 radial lines from

the carbon fiber. The gradient in the modulus values is considerably lower than for 'not post–cured' sample. Specifically, it can be noted that the modulus map begin to increase only close to 100 nm of radial distance from the fiber. This indicates that the width of the interphase region is impacted by the post–curing process which marks an enhanced rate of cross linking reactions.

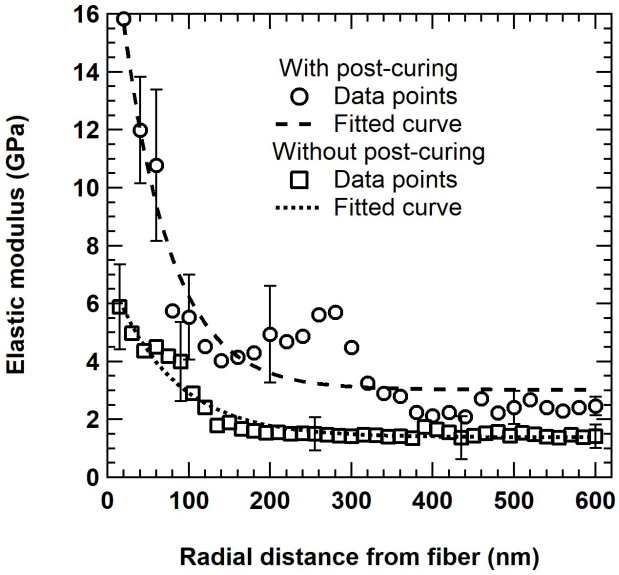

Figure 7.2: Comparison of radial distribution of elastic modulus values of CFRP samples subject to 'post–cured' and 'not post–cured' conditions.

Quantitative study of the variation in the modulus map reveals that there is an increase of 171% in the modulus value at 20 nm away from the fiber for the post–cured samples. However, there is only an increase of about 70% in the modulus value at 600 nm from the fiber. This points to the fact that the presence of carbon fiber influences the post–curing process of epoxy and is an important factor in the development of the interphase region. In this regard, it is important to consider the striking difference in the CTE of the fiber and the matrix which will lead to the presence of residual thermal stress as the material is cooled down after post–curing. The impact of these thermal stresses on the determination of the properties near the fiber can be analyzed using finite element method approach described in chapter 4.

7.3 Finite element modeling of the impact of residual thermal stresses

A complete 3D modeling of the near-fiber region was considered for the FEA analysis, as shown in the fig. 7.3. A circular region of 2.5μm was assigned as the fiber and the surrounding region was modeled to represent the matrix. Hence, the boundary condition assigning one surface of the substrate as a rigid constraint was not used in these simulations. The dimensions of the box region is $6800 \times 6200 \times 900$ nm. These dimensions ensure that the stresses generated from the indentation do not interact with the edge of the substrate. Stresses along a line to the edge were examined in all the directions with a preliminary indentation experiment and it was observed to be zero near the edges. Fiber was assigned properties using engineering constants such as $E_1 = 238$ GPa, $E_2/E_3 = 28$ GPa, $\nu_{12} = 0.28$, $\nu_{13} = 0.02$, $\nu_{23} = 0.33$, $G_{12} = 24$ GPa, $G_{13} = 24$ GPa, $G_{23} = 7.2$ GPa [97]. For the matrix, the elasto–plastic model described in chapter 4 was used. The CTE for the fiber and matrix were assigned as -1.7×10^{-6} and 58×10^{-6}, respectively. Substrate was partitioned at the points of indent with varying distance, 'r' from the periphery of the fiber. Additionally, the partitions were employed to ensure smooth mesh near the region of indent. As noted in the previous chapter, element lengths in the y–direction were kept longer than the other two dimensions to minimize the elemental distortions.

Three steps were used in these simulation. The first step involved the uniform heating of the substrate to 121°C, followed by the second step in which the substrate was cooled to the room temperature of 21°C. Thereafter, indentations were performed at different distances of 600, 400, 200, 100, 80, 60, 40 and 20 nm away from the fiber. All other parameters such as interaction and collection of the output were done similar to FE modeling in the previous chapters. Loading was done using assignment of the boundary condition at the reference point (RP) of the indenter tip in the y–direction for different displacements as determined from the experiments in chapter 3.

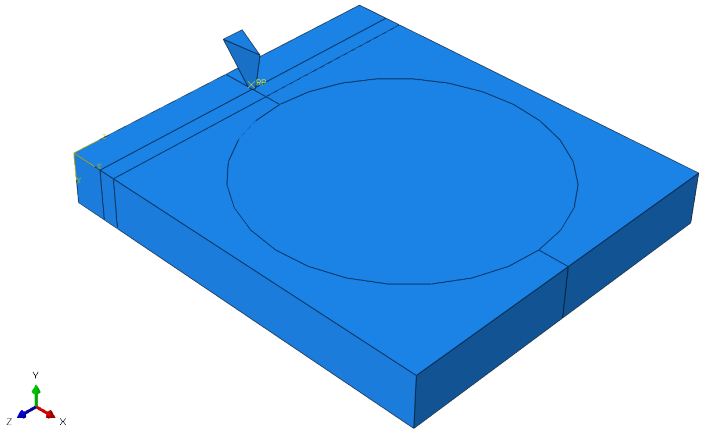

Figure 7.3: 3D representation of the near–fiber region including the fiber and the interphase region.

7.3.1 Radial distribution of elastic modulus

Figure 7.4 shows the variation in the elastic modulus of the region near the fiber determined from the FE model considering the effect of residual thermal stress. The $E_{unconstrained}$ value is lower than the value determined previously in chapter 4. This can be attributed to the presence of resultant tensile stresses that exist from the heating–cooling step prior to the indentation. Also, it can be observed that in the presence of the residual thermal stress there is a gradient in the modulus values determined from the simulations in the region of about 80 nm from the fiber. There is a sharp increase in the modulus value evaluated at 20 nm from the fiber. This is due to the interaction of the stresses developed from the thermal mismatch of the CTEs of the fiber and matrix with the compressive stress produced from indentation. It also suggests that the impact of fiber constraint may also be dependent on the extent of the presence of residual thermal stresses in the interphase region.

The interaction of the stress fields from the indentation with the boundary of the fiber is shown in Fig. 7.5. Reflection of the stress fields produced from the indentation near the fiber gives an apparent increase in the modulus value in the near–fiber region. Results confirm that the presence of thermal stresses in the region near the fiber affects the determination of its properties and likely the fiber constraint effect.

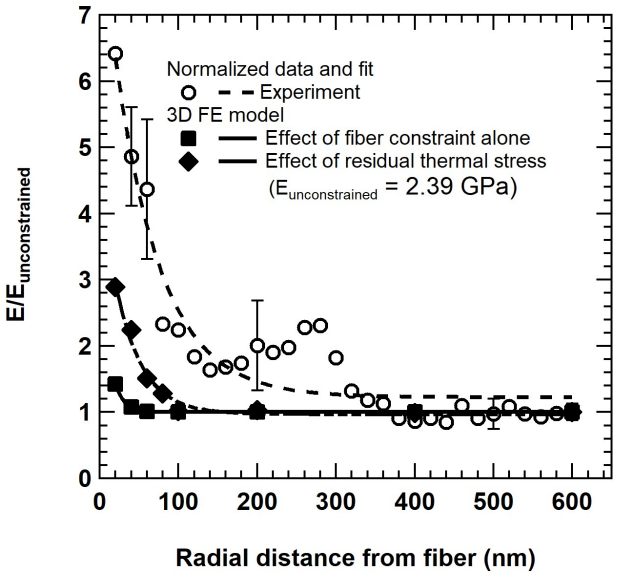

Figure 7.4: Normalized data points and fitted curve of the modulus values along a radial line from FE model considering effect of residual thermal stress.

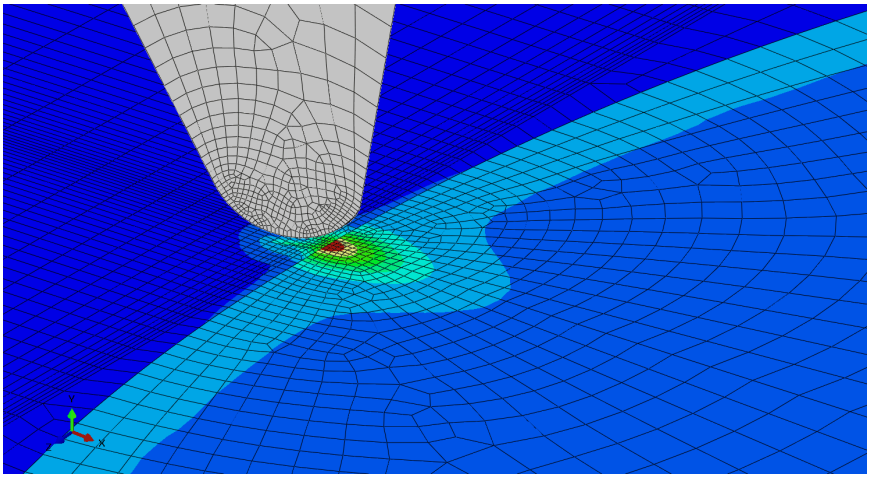

Figure 7.5: Interaction of stress fields from the indentation with the fiber boundary and thermal stresses from heating–cooling step.

Finite element simulations indicate that the nature of the residual thermal stress impacts the modulus value evaluated. Tensile stresses contribute to lowering of the modulus value whereas existence of compressive stress increases the properties. Overall, it is determined that the thermal mismatch between the fiber and the matrix affects the determination of the properties in the near–fiber region.

7.4 Conclusion

AFM indentation based force spectroscopy is used to develop an understanding about the effect of post curing on the formation of the interphase region. Carbon fiber reinforced epoxy samples that were only subject to room temperature curing for 24 hours were analyzed in this study. Modulus map of the interphase region indicates that the unconstrained modulus value is lower than post–cured samples by 70%. Also, it is seen that the effect of post–curing is quite significant in the near–fiber region i.e. post curing leads to an increase of 171% in the modulus value of the region about 20 nm away from the fiber. Additionally, the width of the interphase region evaluated using the radial distribution of modulus value is considerably smaller than the interphase width of a post–cured sample. It highlights the fact that the residual thermal stresses generated from the post curing of the sample at 121°C for 6 hours and subsequent rate of cooling can have a significant impact on the analysis of the interphase region using the approach described in this study.

The influence of the thermal mismatch between the fiber and the matrix on the fiber constraint effect is evaluated using FE simulations. A 3D model with a complete representation of the fiber and the surrounding region is employed to capture the generation of thermal stresses. A heating–cooling step in which the entire substrate is heated to 121°C and thereafter cooled to room temperature of 21°C is utilized to simulate the formation of residual thermal stresses on account of the thermal mismatch and cool down process. An indentation step following the heating–cooling step is used to study the effect on the modulus value at different radial distances from the carbon fiber. Results indicate that the

presence of tensile stresses in the 'unconstrained' region leads to a decrease in the modulus value. However, the thermal mismatch between the fiber and the matrix causes compressive stress to exist in the near–fiber region and hence the modulus value evaluated in this region are significantly higher. A notable finding of these results is the suggestion that the presence of thermal stresses increases the region in which the effect of the fiber constraint on the determination of modulus value.

CHAPTER 8

CONCLUSIONS

8.1 Summary

The aim of this study was to perform a study of the interphase region in the fiber reinforced polymer composites using a combination of experimental and numerical methods. Mechanical characterization of materials using indentation technique has been in use for quite some time due to the availability of closed form solutions to analyze the load–displacement data. However, performing indentation in the near–fiber region represents indentation in a half space constrained by a rigid boundary. This leads to a effect called fiber constraint or fiber bias which causes the stresses produced during the indentation to interact with the the fiber which behaves as rigid boundary due to its elastic modulus being two orders of magnitude higher than the surrounding matrix.

Earlier studies have acknowledged the influence of fiber constraint on the indentation output but didn't contribute to quantifying the impact or decoupling its influence from the true changes in the interphase properties. The only closed form solution that was recently developed based on experimental results was limited by the use of Berkovich nanoindenter tip and circularity of the matrix pockets in which the fiber constraint is analyzed. Employing Berkovich nanoindenter tip to study small interphases such as in carbon fiber reinforced epoxy is limited because of the span of the indentation from small depths being greater than the width of the interphase. Additionally, the effect of fiber constraint has been limited to elasto–plastic behavior till date.

To overcome the problem of analyzing the variations in properties of the interphase region taking into account the effect of fiber constraint, a hybrid approach comprising of

AFM based indentation and FEA simulations can be used to quantify the changes in properties of the interphase region as a function of radial distance to the fiber. It was ascertained that the use of AFM tip will provide the high spatial resolution required to explore the properties of the region very close to the fiber, in the nano–scale. The preliminary step was determined to be the finite element (FE) modeling of Berkovich nanoindentation based on the work done by Hardiman *et al.* [1]. The major changes required in the modeling of the interphase region including the need for a complete 3D representation of the near–fiber region was identified. This implies that assumption of axisymmetry condition for the modeling of interphase region used in some of the previous studies must be omitted as it represents a circular matrix pocket surrounded by a rigid constraint, which is untrue of the interphase region.

In this study, load controlled force spectroscopy using an AFM indenter was employed to evaluate the properties of approximately 1μm region consisting of the carbon fiber and the surrounding epoxy. Adhesion map obtained from the force spectroscopy was used to identify the contour of the fiber and a MATLAB code was developed to extract the modulus values along radial lines from the fiber based on the modulus map data. To investigate the effect of fiber constraint on evaluation of the properties close to the fiber, a 3D FE model of the AFM indentation of the interphase region was created. For obtaining a realistic representation of the interphase region, the specimen was modeled as a 3D block with a rigid curved surface at one end of radius 2.5 μm, representing the carbon fiber. In this regard, the 3D FE model of the AFM indenter was used to find the area function of the indenter.

Analysis of the elastic modulus map of the near–fiber region indicated that there is a gradient in the average elastic modulus values along a radial line to the boundary of the carbon fiber. Using the variation in the modulus value along the radial line, the width of the interphase region was approximated to be 250 nm. Two FE models using an elasto–plastic material definition was employed to study the determination of interphase properties using

AFM indentation. The first model assumed axisymmetry condition and the second model considered a complete 3D representation of the interphase region. Results indicate that assumption of axisymmetry condition leads to a considerable overestimation of the impact of the fiber constraint. From the realistic model, it was noted that the apparent increase in the modulus value due to fiber constraint is limited to a region of 40 nm of radial distance from the fiber. As only a small region is under the influence of fiber constraint and its impact is also significantly lower than the gradient in the near-fiber modulus values, use of inverse analysis technique was determined to be not necessary. Overall, it was demonstrated that the interphase region exhibits distinct behavior in comparison to the bulk matrix.

The influence of fiber constraint on the viscoelastic properties of the interphase region were considered for the first time. A constant displacement based approach was used to obtain the relaxation curves as a function of radial distance to the fiber. Results indicated that there was significant reduction in the relaxation of the material at 20 nm away from the fiber compared to the response of the region at 600 nm from the fiber. This indicates that viscoelastic response of the interphase region is distinct from the bulk material. Furthermore, with aid of two elements of generalized Maxwell model in FE simulations, it was demonstrated that the impact of fiber constraint on the determination of relaxation curves of the interphase region is also limited to a region of 20 nm radial distance from the carbon fiber. It is for the first time, the impact of fiber constraint on the viscoelastic response observed using indentation technique was computed.

AFM indentation based force spectroscopy was also used to examine the effect of environmental factors such as UV irradiation on the interphase properties. Variations in the elastic modulus were studied as a function of radial distance to the fiber and the exposed time to UV irradiation. Results showed that the response of the material was dependent on the proximity to the carbon fiber. For epoxy at 8 mm away from the fiber, chain scissions due to UV exposure led to significant decrease in the elastic modulus. However, for the near–fiber region the modulus initially decreased due to the chain scission and photo–

catalytic degradation of the carbon fiber but subsequently increased due to the increased cross–linking reaction at the newly formed reaction sites. In other words, it can be noted that the presence of carbon fiber hinders the photo-degradation process of epoxy leading to enhanced durability of the composite structure. Evaluation of the viscoelastic response as a function of exposed time showed that the material considerably creep compliant initially, but upon continued exposure to UV irradiation it becomes creep resistant. Unlike the changes in modulus values of the material at 8 mm away from the fiber, epoxy showed significant creep resistance after 6 h of exposure to UV irradiation. This can be possibly attributed to the oxidation of the bulk material or changes in material response upon heating to temperature close to the glass transition temperature.

Another important factor that can influence the variation in the interphase behavior is the thermal mismatch between the coefficient of thermal expansion (CTE) of the carbon fiber and epoxy. A CFRP sample that was only subject to room temperature curing for 24 hours was analyzed using AFM based force spectroscopy and the changes in the elastic modulus were determined. It was observed that the post curing of the sample has significant positive impact on the elastic modulus of the surrounding matrix region and the width of the interphase region. The influence of residual thermal stress from a heating–cooling step on the elastic modulus values of the near–fiber region were determined using FE simulations. It was noted that the presence of thermal stresses considerably increases the region in which the effect of the fiber constraint impact the evaluation of elastic modulus values. The presence of residual tensile stresses from the thermal cycle lowered the modulus value of the region about 600 nm away from the fiber. However, the compressive stress due to the thermal mismatch between the carbon fiber and epoxy contributed to an increase in the modulus value of regions very close to the fiber.

8.2 Major conclusions

Based on the work done in this study, the following points regarding the behavior and characterization of the interphase region can be concluded.

- Properties of interphase region are distinct as determined using the integrated approach based on AFM indentation.
- Interphase thickness in CFRP was observed to be 250nm considering the effect of fiber constraint.
- Axi-symmetry assumption in the modeling of the interphase region leads to overestimation of the effect of fiber constraint and is an incorrect representation of the interphase region.
- Viscoelastic response of the interphase region depends on the proximity to the carbon fiber reinforcement.
- Variations in behavior of interphase region due to UV irradiation is affected by photo-catalytic degradation of carbon fiber, generation of free radicals and subsequent cross-linking reactions.
- Thermal mismatch between carbon fiber and matrix caused by the difference in the coefficient of thermal expansion impacts the interphase thickness and extend of influence of fiber constraint effect.

8.3 Recommendations

The combination of AFM indentation and FE modeling has been shown as a powerful tool to characterize regions of very small length scales and determine the influences of various parameters on the properties of the region. This approach improves the understanding about the effect of indentations carried out in a non-uniform half space. By providing an

extended analysis of the interphase region in carbon fiber reinforced epoxy, knowledge about the importance of presence of carbon fiber in terms of the durability of the composite was established. Further studies involving sub–surface structure and chemical interactions at nano–scale will be beneficial to examine the complete mechanism of formation of the interphase region and effects of different factors on the properties of this important region. In this regard, the following are recommended to be valuable additions in the characterization of the interphase region of fiber reinforced polymer composites and the use of the technique harnessed in this study.

- Examine the impact of stochastic distribution of carbon fiber on the effect of fiber constraint.
- Model the interphase region using concentric circular regions with gradient in elastic modulus - to help FEA mimic experimental results.
- Demonstrate the use of the developed technique to examine individual domains in mixed matrix membranes.
- Development of an AFM integrated tool to investigate chemical changes occurring in nano-scale regions.

BIBLIOGRAPHY

[1] M. Hardiman, T. J. Vaughan, and C. T. McCarthy, "The effect of fibre constraint in the nanoindentation of fibrous composite microstructures: A finite element investigation," *Computational Materials Science*, vol. 64, pp. 162–167, 2012.

[2] B. Mailhot, S. Morlat-Thérias, M. Ouahioune, and J. L. Gardette, "Study of the degradation of an epoxy/amine resin, 1 photo- and thermo-chemical mechanisms," *Macromolecular Chemistry and Physics*, vol. 206, pp. 575–584, 2005.

[3] B. E. B. Uribe, E. M. S. Chiromito, A. J. F. Carvalho, R. Arenal, and J. R. Tarpani, "TEMPO-oxidized cellulose nanofibers as interfacial strengthener in continuous-fiber reinforced polymer composites," *Materials and Design*, vol. 133, pp. 340–348, 2017.

[4] D. Kada, A. Koubaa, G. Tabak, S. Migneault, B. Garnier, and A. Boudenne, "Tensile properties, thermal conductivity, and thermal stability of short carbon fiber reinforced polypropylene composites," *Polymer Composites*, vol. 39, no. S2, pp. E664–E670, 2016.

[5] P. Xu, Y. Yu, D. Liu, M. He, G. Li, and X. Yang, "Enhanced interfacial and mechanical properties of high-modulus carbon fiber composites: Establishing modulus intermediate layer between fiber and matrix based on tailored-modulus epoxy," *Composites Science and Technology*, vol. 163, pp. 26–33, 2018.

[6] N. Kotelnikova-Weiler, O. Baverel, N. Ducoulombier, and J. F. Caron, "Progressive damage of a unidirectional composite with a viscoelastic matrix, observations and modelling," *Composite Structures*, vol. 188, pp. 297–312, 2018.

[7] Y. Niu, Y. Yang, and X. Wang, "Investigation of the interphase structures and properties of carbon fiber reinforced polymer composites exposed to hydrothermal treatments using peak force quantitative nanomechanics technique," *Polymer Composites*, vol. 39, no. S2, pp. E791–E796, 2018.

[8] R. M. Guedes, J. J. L. Morais, A. Nio, T. Marques, and A. H. Cardon, "Prediction of long-term behaviour of composite materials," *Computers and Structures*, vol. 76, pp. 183–194, 2000.

[9] L. Drzal, "Composite interphase characterization," in *SAMPE Journal*, vol. Vol 19, pp. 7–13, 1983.

[10] L. T. Drzal, "The interphase in epoxy composites," *Epoxy Resins and Composites II*, pp. 1–32, 1986.

[11] M. Vanlandingham, S. McKnight, G. Palmese, T. Bogetti, R. Eduljee, and J. Gillespie, "Characterization of Interphase Regions Using Atomic Force Microscopy," in *MRS Proceedings*, p. 458., 1996.

[12] H. Gajendran, R. B. Hall, A. Masud, and K. R. Rajagopal, "Chemo-mechanical coupling in curing and material-interphase evolution in multi-constituent materials," *Acta Mechanica*, vol. 217, pp. 1–22, 2018.

[13] T. A. Bogetti, T. Wang, M. R. Vanlandingham, and J. W. Gillespie, "Characterization of nanoscale property variations in polymer composite systems: 2. Numerical modeling," *Composites Part A*, vol. 30, pp. 85–94, 1999.

[14] W. Xu, F. Wu, Y. Jiao, and M. Liu, "A general micromechanical framework of effective moduli for the design of nonspherical nano- and micro-particle reinforced composites with interface properties," *Materials and Design*, vol. 127, pp. 162–172, 2017.

[15] J. Karger-Kocsis, H. Mahmood, and A. Pegoretti, "Recent advances in fiber/matrix interphase engineering for polymer composites," *Progress in Materials Science*, vol. 73, pp. 1–43, 2015.

[16] M. D. R. Batista and L. T. Drzal, "Carbon fiber/epoxy matrix composite interphases modified with cellulose nanocrystals," *Composites Science and Technology*, vol. 164, pp. 274–281, 2018.

[17] V. Cech, E. Palesch, and J. Lukes, "The glass fiber-polymer matrix interface/interphase characterized by nanoscale imaging techniques," *Composites Science and Technology*, vol. 83, pp. 22–26, 2013.

[18] Y. Gu, M. Li, J. Wang, and Z. Zhang, "Characterization of the interphase in carbon fiber/polymer composites using a nanoscale dynamic mechanical imaging technique," *Carbon*, vol. 48, no. 11, pp. 3229–3235, 2010.

[19] A. Valadez-Gonzalez, J. M. Cervantes-Uc, R. Olayo, and P. J. Herrera-Franco, "Effect of fiber surface treatment on the fiber-matrix bond strength of natural fiber reinforced composites," *Composites Part B*, vol. 30, pp. 309–320, 1999.

[20] K. Mishra, G. Pandey, and R. P. Singh, "Enhancing the mechanical properties of an epoxy resin using polyhedral oligomeric silsesquioxane (POSS) as nanoreinforcement," *Polymer Testing*, vol. 62, pp. 210–218, 2017.

[21] K. Mishra and R. P. Singh, "Effect of APTMS modification on multiwall carbon nanotube reinforced epoxy nanocomposites," *Composites Part B: Engineering*, vol. 162, pp. 425–432, 2019.

[22] K. Mishra and R. P. Singh, "Quantitative evaluation of the effect of dispersion techniques on the mechanical properties of polyhedral oligomeric silsesquioxane (POSS)-epoxy nanocomposites," *Polymer Composites*, vol. 39, pp. E2445–E2453, 2018.

[23] D. R. Dhakal, P. Lamichhane, K. Mishra, T. L. Nelson, and R. K. Vaidyanathan, "Influence of graphene reinforcement in conductive polymer: Synthesis and characterization," *Polymers for Advanced Technologies*, pp. 1–11, 2019.

[24] K. Mishra, K. P. Bastola, R. P. Singh, and R. Vaidyanathan, "Effect of graphene oxide on the interlaminar fracture toughness of carbon fiber/epoxy composites," *Polymer Engineering and Science*, pp. 1–10, 2019.

[25] K. Herrman, L. N. Baxter, K. Mishra, E. Benton, R. P. Singh, and R. K. Vaidyanathan, "Mechanical characterization of polyethylene-based thermoplastic composite materials for radiation shielding," *Composites Communications*, vol. 13, pp. 37–41, 2019.

[26] A. M. Díez-Pascual, M. A. Gómez-Fatou, F. Ania, and A. Flores, "Nanoindentation assessment of the interphase in carbon nanotube-based hierarchical composites," *Journal of Physical Chemistry C*, vol. 116, pp. 24193–24200, 2012.

[27] R. F. Gibson, "A review of recent research on nanoindentation of polymer composites and their constituents," *Composites Science and Technology*, vol. 105, pp. 51–65, 2014.

[28] A. Molazemhosseini, H. Tourani, M. R. Naimi-Jamal, and A. Khavandi, "Nanoindentation and nanoscratching responses of PEEK based hybrid composites reinforced with short carbon fibers and nano-silica," *Polymer Testing*, vol. 32, no. 3, pp. 525–534, 2013.

[29] T. J. Young, L. E. Crocker, W. R. Broughton, S. L. Ogin, and P. A. Smith, "Observations on interphase characterisation in polymer composites by nano-scale indentation using AFM and FEA," *Composites Part A: Applied Science and Manufacturing*, vol. 50, pp. 39–43, 2013.

[30] L. Belec and Y. Joliff, "Mechanically affected zone in AFM force measurements - Focus on actual probe tip geometry," *Materials and Design*, vol. 104, pp. 217–226, 2016.

[31] D. Wang and T. P. Russell, "Advances in Atomic Force Microscopy for Probing Polymer Structure and Properties," *Macromolecules*, vol. 51, no. 1, pp. 3–24, 2018.

[32] T. Downing, R. Kumar, W. Cross, L. Kjerengtroen, and J. Kellar, "Determining the interphase thickness and properties in polymer matrix composites using phase imaging atomic force microscopy and nanoindentation," vol. 14, pp. 1801–1812, 2000.

[33] C. Griswold, W. M. Cross, L. Kjerengtroen, and J. J. Kellar, "Interphase variation in silane-treated glass-fiber- reinforced epoxy composites," *J. Adhesion Sci. Technol*, vol. 19, pp. 3–5, 2005.

[34] W. Oliver and G. Pharr, "An improved technique for determining hardness and elastic modulus using load and displacement sensing indentation experiments," *Journal of Materials Research*, vol. 7, no. 6, pp. 1564–1583, 1992.

[35] M. Munz, H. Sturm, E. Schulz, and G. Hinrichsen, "The scanning force microscope as a tool for the detection of local mechanical properties within the interphase of fibre reinforced polymers," *Composites Part A*, vol. 29A, pp. 1251–1259, 1998.

[36] J. Kim, M. Sham, and J. Wu, "Nanoscale characterisation of interphase in silane treated glass fibre composites," *Composites Part A: Applied Science and Manufacturing*, vol. 32, pp. 607–618, 2001.

[37] S. H. Lee, S. Wang, G. M. Pharr, and H. Xu, "Evaluation of interphase properties in a cellulose fiber-reinforced polypropylene composite by nanoindentation and finite element analysis," *Composites Part A: Applied Science and Manufacturing*, vol. 38, pp. 1517–1524, 2007.

[38] Y. Wang and T. H. Hahn, "AFM characterization of the interfacial properties of carbon fiber reinforced polymer composites subjected to hygrothermal treatments," *Composites Science and Technology*, vol. 67, pp. 92–101, 2007.

[39] C. Reynaud, F. Sommer, C. Quet, N. E. Bounia, and T. M. Duc, "Quantitative determination of Young's modulus on a biphase polymer system using atomic force microscopy," *Surface and Interface Analysis*, vol. 30, pp. 185–189, 2000.

[40] I. N. Sneddon, "The relation between load and penetration in the axisymmetric boussinesq problem for a punch of arbitrary profile," *International Journal of Engineering Science*, vol. 3, no. 1, pp. 47–57, 1965.

[41] M. F. Doerner and W. D. Nix, "A method for interpreting the data from depth-sensing indentation instruments," *Journal of Materials Research*, vol. 1, no. 4, pp. 601–609, 1986.

[42] G. Feng and A. H. Ngan, "Effects of creep and thermal drift on modulus measurement using depth-sensing indentation," *Journal of Materials Research*, vol. 17, no. 3, pp. 660–668, 2002.

[43] R. Kumar, W. M. Cross, L. Kjerengtroen, and J. J. Kellar, "Fiber bias in nanoindentation of polymer matrix composites," *Composite Interfaces*, vol. 11, no. 56, pp. 431–440, 2004.

[44] A. M. Díez-Pascual, M. A. Gómez-Fatou, F. Ania, and A. Flores, "Nanoindentation in polymer nanocomposites," *Progress in Materials Science*, vol. 67, pp. 1–94, 2015.

[45] Y. Li, M. Li, Y. Gu, Z. Zhang, and P. Guan, "Investigation of the nanoscale mechanical properties of carbon fiber/epoxy resin interphase. I. analysis of fiber-stiffening effect during the nanoindentation process based on numerical simulation," *Polymer Composites*, vol. 33, no. 8, pp. 1387–1394, 2012.

[46] S. K. Khanna, P. Ranganathan, S. B. Yedla, R. M. Winter, and K. Paruchuri, "Investigation of nanomechanical properties of the interphase in a glass fiber reinforced polyester composite using nanoindentation," *Journal of Engineering Materials and Technology*, vol. 125, no. 2, pp. 90–96, 2003.

[47] F. Li, J. G. Williams, B. S. Altan, I. Miskioglu, and R. L. Whipple, "Studies of the interphase in epoxy-aluminum joints using nano-indentation and atomic force microscopy," *Journal of Adhesion Science and Technology*, vol. 16, no. 7, pp. 935–949, 2002.

[48] Z. Hu, K. J. Lynne, S. P. Markondapatnaikuni, and F. Delfanian, "Material elastic-plastic property characterization by nanoindentation testing coupled with computer modeling," *Materials Science and Engineering A*, vol. 587, pp. 268–282, 2013.

[49] Z. Hu, M. Farahikia, and F. Delfanian, "Fiber bias effect on characterization of carbon fiber-reinforced polymer composites by nanoindentation testing and modeling," *Journal of Composite Materials*, vol. 49, no. 27, pp. 3359–3372, 2015.

[50] M. Hardiman, T. J. Vaughan, and C. T. McCarthy, "Fibrous composite matrix characterisation using nanoindentation: The effect of fibre constraint and the evolution from bulk to in-situ matrix properties," *Composites: Part A*, vol. 68, pp. 296–303, 2015.

[51] P. F. Brune, G. S. Blackman, T. Diehl, J. S. Meth, D. Brill, Y. Tao, and J. Thornton, "Direct Measurement of Rubber Interphase Stiffness," *Macromolecules*, vol. 49, no. 13, pp. 4909–4922, 2016.

[52] S. Roy, J. Ryan, S. Webster, and D. Nepal, "A Review of In-Situ Mechanical Characterization of Polymer Nanocomposites," *Applied Mechanics Reviews*, vol. 69, no. 050802, pp. 1–18, 2017.

[53] Y. Wang, Y. Zhang, H. Zhao, X. Li, Y. Huang, L. S. Schadler, W. Chen, and L. C. Brinson, "Identifying interphase properties in polymer nanocomposites using adaptive optimization," *Composites Science and Technology*, vol. 162, pp. 146–155, 2018.

[54] D. Tranchida, Z. Kiflie, S. Acierno, and S. Piccarolo, "Nanoscale mechanical characterization of polymers by atomic force microscopy (AFM) nanoindentations: Viscoelastic characterization of a model material," *Measurement Science and Technology*, vol. 20, no. 095702, pp. 1–9, 2009.

[55] B. G. Kumar, R. P. Singh, and T. Nakamura, "Degradation of Carbon Fiber-reinforced Epoxy Composites by Ultraviolet Radiation and Condensation," *Journal of Composite Materials*, vol. 36, no. 24, pp. 2713–2721, 2002.

[56] Y. F. Niu, Y. Yang, T. Y. Li, and J. W. Yao, "Effects of UV irradiation and condensation on poly(ether-ether-ketone)/carbon fiber composites from nano- to macro-scale," *High Performance Polymers*, vol. 30, no. 2, pp. 230–238, 2018.

[57] Y. F. Niu, Y. Yang, S. Gao, and J. W. Yao, "Mechanical mapping of the interphase in carbon fiber reinforced poly(ether-ether-ketone) composites using peak force atomic force microscopy: Interphase shrinkage under coupled ultraviolet and hydro-thermal exposure," *Polymer Testing*, vol. 55, pp. 257–260, 2016.

[58] K. Mishra, S. Das, and R. Vaidyanathan, "The Use of Recycled Carpet in Low-Cost Composite Tooling Materials," *Recycling*, vol. 4, no. 1, pp. 1–12, 2019.

[59] K. Mishra and R. Vaidyanathan, "The Influence of Nanoclay on the Flame Retardancy and Mechanical Performance of Recycled Carpet Composites," *Recycling*, vol. 4, no. 2, pp. 1–10, 2019.

[60] F. Awaja and P. J. Pigram, "Surface molecular characterisation of different epoxy resin composites subjected to UV accelerated degradation using XPS and ToF-SIMS," *Polymer Degradation and Stability*, vol. 94, pp. 651–658, 2009.

[61] H. Li, Y. Wang, C. Zhang, and B. Zhang, "Effects of thermal histories on interfacial properties of carbon fiber/polyamide 6 composites: Thickness, modulus, adhesion and shear strength," *Composites Part A: Applied Science and Manufacturing*, vol. 85, pp. 31–39, 2016.

[62] J. Moosburger-Will, J. Jäger, J. Strauch, M. Bauer, S. Strobl, F. F. Linscheid, and S. Horn, "Interphase formation and fiber matrix adhesion in carbon fiber reinforced epoxy resin: influence of carbon fiber surface chemistry," *Composite Interfaces*, vol. 24, no. 7, pp. 691–710, 2017.

[63] K. Dong, J. Zhang, M. Cao, M. Wang, B. Gu, and B. Sun, "A mesoscale study of thermal expansion behaviors of epoxy resin and carbon fiber/epoxy unidirectional composites based on periodic temperature and displacement boundary conditions," *Polymer Testing*, vol. 55, pp. 44–60, 2016.

[64] J. Dean, G. Aldrich-Smith, and T. W. Clyne, "Use of nanoindentation to measure residual stresses in surface layers," *Acta Materialia*, vol. 59, no. 7, pp. 2749–2761, 2011.

[65] J. E. Sader, J. W. M. Chon, and P. Mulvaney, "Calibration of rectangular atomic force microscope cantilevers," *Review of Scientific Instruments*, vol. 70, no. 10, pp. 3967–3969, 1999.

[66] L. K. Babu, K. Mishra, and R. P. Singh, "Near-fiber effects of UV irradiation on the fiber-matrix interphase: A combined experimental and numerical investigation," *Materials and Design*, vol. 157, pp. 294–302, 2018.

[67] ASTM International, "ASTM D 695 - 15 Compressive Properties of Rigid Plastics," tech. rep., 2015.

[68] M. T. Shaw and W. J. MacKnight, *Introduction to polymer viscoelasticity*. John Wiley & Sons, 4th ed. ed., 2018.

[69] H. Brinson and L. Brinson, *Polymer Engineering Science and Viscoelasticity - An Introduction*. Springer, second ed., 2008.

[70] J. A. Forrest, K. Dalnoki-Veress, J. R. Stevens, and J. R. Dutcher, "Effect of free surfaces on the glass transition temperature of thin polymer films," *Physical Review Letters*, vol. 77, no. 10, pp. 2002–2005, 1996.

[71] A. Hu, X. Li, A. Ajdari, B. Jiang, C. Burkhart, W. Chen, and L. C. Brinson, "Computational analysis of particle reinforced viscoelastic polymer nanocomposites - statistical study of representative volume element," *Journal of the Mechanics and Physics of Solids*, vol. 114, pp. 55–74, 2018.

[72] F. T. Fisher and L. C. Brinson, "Viscoelastic interphases in polymer-matrix composites: Theoretical models and finite-element analysis," *Composites Science and Technology*, vol. 61, no. 5, pp. 731–748, 2001.

[73] J. Li and G. J. Weng, "Effect of a viscoelastic interphase on the creep and stress/strain behavior of fiber - reinforced polymer matrix composites," *Composites Part B*, vol. 27B, pp. 589–598, 1996.

[74] L. Liu, C. Jia, J. He, F. Zhao, D. Fan, L. Xing, M. Wang, F. Wang, Z. Jiang, and Y. Huang, "Interfacial characterization, control and modification of carbon fiber reinforced polymer composites," *Composites Science and Technology*, vol. 121, pp. 56–72, 2015.

[75] D. Tranchida, S. Piccarolo, J. Loos, and A. Alexeev, "Mechanical characterization of polymers on a nanometer scale through nanoindentationn. A study on pile-up and viscoelasticity," *Macromolecules*, vol. 40, no. 4, pp. 1259–1267, 2007.

[76] M. R. Vanlandingham, J. S. Villarrubia, W. F. Guthrie, and G. F. Meyers, "Nanoidentation of Polymers: An Overview," vol. 167, pp. 15–43, 2001.

[77] M. Beyaoui, P. Mazeran, M. Arvieu, M. Bigerelle, and M. Guigon, "Analysis of nanoindentation curves in the case of bulk amorphous polymers," *International Journal of Materials Research*, vol. 100, pp. 943–949, 2009.

[78] M. Hardiman, T. J. Vaughan, and C. T. McCarthy, "The effects of pile-up, viscoelasticity and hydrostatic stress on polymer matrix nanoindentation," *Polymer Testing*, vol. 52, pp. 157–166, 2016.

[79] L. K. Babu, K. Mishra, S. U. Hamim, and R. P. Singh, "Effect of excess silane on the viscoelastic behavior of epoxy under hygrothermal conditions," *International Journal of Adhesion and Adhesives*, vol. 84, pp. 80–85, 2018.

[80] G. Hochstetter, A. Jimenez, and J. L. Loubet, "Strain-rate effects on hardness of glassy polymers in the nanoscale range. Comparison between quasi-static and continuous stiffness measurements," *Journal of Macromolecular Science, Part B*, vol. 38, no. 5-6, pp. 681–692, 1999.

[81] G. Huang, B. Wang, and H. Lu, "Measurements of viscoelastic functions of polymers in the frequency-domain using nanoindentation," *Mechanics of Time-Dependent Materials*, vol. 8, no. 4, pp. 345–364, 2004.

[82] C. C. White, M. R. Vanlandingham, P. L. Drzal, N. K. Chang, and S. H. Chang, "Viscoelastic characterization of polymers using instrumented indentation. II. Dynamic testing," *Journal of Polymer Science: Part B: Polymer Physics*, vol. 43, no. 14, pp. 1812–1824, 2005.

[83] G. Huang and H. Lu, "Measurement of Young's relaxation modulus using nanoindentation," *Mechanics of Time-Dependent Materials*, vol. 10, no. 3, pp. 229–243, 2006.

[84] C. A. Tweedie and K. J. Van Vliet, "Contact creep compliance of viscoelastic materials via nanoindentation," *Journal of Materials Research*, vol. 21, no. 6, pp. 1576–1589, 2006.

[85] M. Vandamme, C. A. Tweedie, G. Constantinides, F. J. Ulm, and K. J. Van Vliet, "Quantifying plasticity-independent creep compliance and relaxation of viscoelastoplastic materials under contact loading," *Journal of Materials Research*, vol. 27, no. 1, pp. 302–312, 2012.

[86] M. Zhai and G. B. McKenna, "Mechanical and viscoelastic properties of polymer thin films and surfaces," in *Polymer Glasses*, pp. 221–258, 2016.

[87] S. Shimizu, T. Yanagimoto, and M. Sakai, "Pyramidal indentation load-depth curve of viscoelastic materials," *Journal of Materials Research*, vol. 14, no. 10, pp. 4075–4086, 1999.

[88] R. S. C. Woo, H. Zhu, C. K. Y. Leung, and J. K. Kim, "Environmental degradation of epoxy-organoclay nanocomposites due to UV exposure: Part II residual mechanical properties," *Composites Science and Technology*, vol. 68, pp. 2149–2155, 2008.

[89] Y. Mulyana, M. Uenuma, Y. Ishikawa, and Y. Uraoka, "Reversible oxidation of graphene through ultraviolet/ozone treatment and its nonthermal reduction through ultraviolet irradiation," *The Journal of Physical Chemistry C*, vol. 118, no. 47, pp. 27372–27381, 2014.

[90] S. U. Hamim, K. Mishra, and R. P. Singh, "Effect of UV Exposure on Mechanical Properties of POSS Reinforced Epoxy Nanocomposites," in *Challenges in Mechanics of Time-Dependent Materials, Vol. 2*, pp. 147–152, Springer International Publishing, 2015.

[91] K. Jayaraman and K. L. Reifsnider, "The interphase in unidirectional fiber-reinforced epoxies: Effect on residual thermal stresses," *Composites Science and Technology*, vol. 47, no. 2, pp. 119–129, 1993.

[92] Y. Guo, Y. Wang, G. Guo, and Y. Xie, "Finite element analysis of the thermal residual stress distribution in the interphase of unidirectional fiber-reinforced resin matrix composites," *Composite Interfaces*, vol. 25, no. 9, pp. 823–838, 2018.

[93] L. Penn, F. Bystry, W. Karp, and S. Lee, "Aramid/Epoxy vs Graphite/Epoxy: Origin of the difference in strength at the interface," in *Molecular characterization of composite interfaces*, pp. 93–109, Springer, 1985.

[94] T. J. Vaughan and C. T. McCarthy, "Micromechanical modelling of the transverse damage behaviour in fibre reinforced composites," *Composites Science and Technology*, vol. 71, no. 3, pp. 388–396, 2011.

[95] L. G. Zhao, N. A. Warrior, and A. C. Long, "A micromechanical study of residual stress and its effect on transverse failure in polymer-matrix composites," *International Journal of Solids and Structures*, vol. 43, no. 18-19, pp. 5449–5467, 2006.

[96] V. Teimouri and M. Safarabadi, "Finite element prediction of curing micro-residual stress distribution in polymeric composites considering hybrid interphase region," *Engineering Solid Mechanics*, pp. 11–20, 2017.

[97] M. Hardiman, T. J. Vaughan, and C. T. McCarthy, "The effect of microscale residual stress from thermal cooldown on the nanoindentation properties of fibre-reinforced composites," *Journal of Composite Materials*, vol. 50, no. 29, pp. 4147–4158, 2016.

APPENDIX

```
clear;
clc;
filename = 'uv6hr_1.xlsx';
sheet = 'Sheet1';
sheet1 = 'Sheet2';
sheet2 = 'Sheet3';
sheet3 = 'Sheet4';
sheet4 = 'Sheet5';
data = xlsread(filename,sheet,'A1:AV48');
cx = xlsread(filename,sheet1,'A1:A55');
cy = xlsread(filename,sheet1,'B1:B55');
matx=data(:,:);      % Reading data from matrix
x = cx(:);% point on circle
y = cy(:);
[xc,yc,R,a] = circfit(x,y); % Finding center and radius
i=0; j=48;
x2 =1; x1=0; y2=30; y1=0;
count =1;
m=1; n=1; p=1; q=1; v=1;
t=1; u=1;
e=1; f=1;
%xlswrite(filename,matx(x2,y2),sheet2,'A1'); % Printing P1
for i=0:360          % for finding relevant points on the circle
    thet = deg2rad(i);
    x = xc + (R* cos(thet));
    y = yc + (R* sin(thet));
    x1=round(x);
    y1=round(y);
    %if count == 1 % count is for avoiding multiple print of same data
    if(x1 >= 1 && x1 <= 48) && (y1 >=1 && y1 <= 48)
        pcircle(m,n)=matx(x1,y1);
        n=n+1;
        xcirc(v)=x1;
        ycirc(v)=y1;
        v=v+1;
        %count = count + 1;
        s = (yc-y1)/(xc-x1);
        d = y1-(s*x1);
        for j=x1:48
            for k=y1:48
                yr=(s*j)-d;
                yt=round(yr);
                if yt == k
                    nline(p,q)=matx(j,k);
                    coordx(t,u)=j;
                    t=t+1;
                    coordy(e,f)=k;
                    e=e+1;
                    p=p+1;
                end
                k=k+1;
            end
            j=j+1;
        end
        q=q+1;
        u=u+1;
        f=f+1;
        t=1;e=1;
      end

end
i=i+1;
xlswrite(filename,coordx,sheet3,'A1');
xlswrite(filename,coordy,sheet4,'A1');
xlswrite(filename,xcirc,sheet1,'G1');
xlswrite(filename,ycirc,sheet1,'G2');
xlswrite(filename,pcircle,sheet2,'B1'); % Print all the points found on circle
xlswrite(filename,nline,sheet2,'B2');
```

```
function   [xc,yc,R,a] = circfit(x,y)
%
%   [xc yx R] = circfit(x,y)
%
%   fits a circle  in x,y plane in a more accurate
%  procedure than circfit2 but using more memory
%  x,y are column vector where (x(i),y(i)) is a measured point
%  result is center point (yc,xc) and radius R
%  an optional output is the vector of coefficient a
% describing the circle's equation
%   x^2+y^2+a(1)*x+a(2)*y+a(3)=0
%  By:  Izhak bucher 25/oct /1991,
    x=x(:); y=y(:);
   a=[x y ones(size(x))]\[-(x.^2+y.^2)];
   xc = -.5*a(1);
   yc = -.5*a(2);
   R  =  sqrt((a(1)^2+a(2)^2)/4-a(3));
```

VITA

Libin Kaleeluvilayil Babu

Candidate for the Degree of

Doctor of Philosophy

Dissertation: The Use of AFM Indentation to Quantify Mechanical Properties of the Interphase Region in Fiber- reinforced Composites

Major Field: Mechanical Engineering

Biographical:

Personal Data: Born in Adoor, Kerala, India on February 15th 1990.

Education:

Completed the requirements for the Doctor of Philosophy with a major in Mechanical and Aerospace Engineering at Oklahoma State University, Tulsa, Oklahoma in July, 2019.

Received Master of Science degree with a major in Mechanical and Aerospace Engineering from Oklahoma State University, Stillwater, Oklahoma in July, 2015.

Received B.Tech. degree with a major in Mechanical Engineering from University of Kerala, Thiruvananthapuram, Kerala, India in May, 2012.

Experience:

Worked as a Graduate Research Assistant at the Mechanics of Advanced Materials Laboratory headed by Dr. Raman P. Singh in the area of fiber reinforced polymer composites.